Two- and three-dimensional stability of an inlet-modulated radial swirling source flow between parallel annular plates

Meng Fan *
School of Electrical, Energy and Power Engineering, Yangzhou University, Yangzhou 225127, Jiangsu, China and Université Lille, CNRS, ONERA, Arts et Métiers Institute of Technology, Centrale Lille, UMR 9014-LMFL-Laboratoire de Mécanique des Fluides de Lille - Kampé de Fériet, 59655 Villeneuve d'Ascq, France

Antoine Dazin , Gérard Bois , and Francesco Romanò
Université Lille, CNRS, ONERA, Arts et Métiers Institute of Technology, Centrale Lille, UMR 9014-LMFL-Laboratoire de Mécanique des Fluides de Lille - Kampé de Fériet, 59655 Villeneuve d'Ascq, France

(Received 8 October 2025; accepted 17 July 2026; published 10 August 2026)

The turbulent radial flow between parallel annular plates of finite span is studied with a focus on instabilities induced by a periodically modulated swirling source inflow. This investigation utilizes a combination of theoretical modeling along with simplified two- and three-dimensional numerical simulations. Different levels of complexity gradually evolve in the radial diffuser model to identify the different instabilities and to trace back the instabilities to different physical mechanisms. First, a linear stability analysis is performed for a two-dimensional core-flow instability mechanism on a one-dimensional basic state, considering the flow to be inviscid and homogeneous in the azimuthal θ direction. Following this, several two-dimensional numerical simulations are conducted, including viscous effects, nonlinear effects, and inflow modulation in the azimuthal direction. Finally, three-dimensional numerical simulations are carried out to evaluate the impact of the boundary layer on the instabilities.

DOI: 10.1103/pys5-btyx

I. INTRODUCTION

Radial flow between parallel annular plates is considered a fundamental problem in fluid dynamics that involves radial expansion [1,2] and diffusion [3,4], depending on whether the flow originates from or converges toward the axis. This problem has practical applications in many engineering fields, including radial diffusers [5–7], radial flow nozzles [8], double disk valves [9], and thrust bearings [10], and even in some natural phenomena, including the outflow from geothermal energy reservoirs [11] and soil chemical processes [12]. These flows are characterized by complex interactions between inertial, viscous, and centrifugal forces, which can lead to a range of flow regimes from laminar to turbulent flow, with flow separation and reattachment. When centrifugal forces dominate, the flow may exhibit instabilities, breaking temporal and spatial symmetries. Conversely, if viscous forces are more significant, the flow might transition to a creeping or fully laminar regime, especially as the flow moves outward and inertial forces diminish.

Several researchers have investigated instabilities in parallel radial flow, with some identifying the presence of inflection points [13,14] and the phenomena of self-sustained separation and

*Contact author: meng.fan@yzu.edu.cn

reattachment of shear layers [15]. Our study concentrates on turbulent source flow between parallel annular plates of finite span, with a particular emphasis on the instabilities that arise from a swirling source inflow that is periodically modulated in space and time, intending to reveal the fundamental physics of the instabilities. Such instabilities can develop in radial diffusers, which are commonly placed downstream of the impeller of centrifugal pumps and compressors. The role of this part is to convert a part of the kinetic energy given to the fluid in the runner into static pressure and enthalpy. The study of the development of instabilities in radial diffusers is of important applicative interest because these phenomena (often referred to in the literature as "diffuser rotating stall") often trigger the whole compressing system to surge [16], which can have disastrous effects on the machine itself or its environment [17]. Various authors investigated the rotating instabilities in the radial vaneless diffuser of centrifugal machines [18–22]. Theoretical studies are mainly based on two different approaches:

(i) three-dimensional stability analysis of the wall boundary layer for narrow vaneless diffusers [18,23–26];

(ii) two-dimensional methods utilizing inviscid core-flow to examine the stability of wide vaneless diffusers [19,22,27–29].

Numerical and experimental studies are also performed by several researchers [5–7,20,21], indicating that no single geometric parameter definitively suggests that wide and narrow vaneless diffusers exhibit different instability mechanisms. While these studies improved our understanding of unsteady phenomena, they do not offer a coherent characterization of the various instabilities that may arise in turbulent vaneless diffuser flow with a periodically spatially modulated source inflow rotating at an angular velocity Ω. Therefore, our study aims to extend the previous investigations by conducting a comprehensive theoretical and numerical characterization.

In our previous experimental and numerical study [30–34], the inflow boundary condition was generated by employing a seven-blade device rotating at a constant rate Ω. Two different instability regions were identified at large and small flow rates. To provide evidence of these two identified instabilities and to trace back the instabilities to different physical mechanisms, we propose to consider canonical flow and progressively evolve it in different levels of complexity as follows:

(i) First, a linear stability analysis (LSA) is carried out for the inviscid logarithmic spiral core flow with a homogeneous inlet. The formulation details are presented in Sec. II C and the results are reported in Sec. IV A. Note that the LSA of a radial diffuser and the corresponding energy budget have already been successfully employed in our earlier publication [33] for rationalizing the Fourier mode 3 ($m = 3$) instability identified in our previous experiments and simulations of a full centrifugal machine model. Our previous study was limited to a single inlet-to-outlet radius ratio and studied only three-periodic perturbations. Significantly extending beyond that work, the present study conducts a comprehensive LSA for three different inlet-to-outlet radius ratios of the radial diffuser (midplane section at midheight between the parallel annular plates), considering instability Fourier-mode numbers from $m = 1$ to $m = 16$.

(ii) Second, we carry out two-dimensional numerical simulations with a swirling radial source inlet periodically modulated in space and time. The inflow modulation strategy was originally tested in three dimensions in our earlier work [32], showing promising predictive capabilities for studying the instability. We use it here first in two-dimensional flows because we aim to rationalize the inlet-flow role over two-dimensional instability mechanisms. We recall the details of this approach in Sec. II B, and then report the corresponding results in Sec. IV B. Several qualitatively different inflows are considered with the aim of making a conclusive statement on the role of a swirling inflow in the two-dimensional destabilization mechanisms. We also conduct a systematic investigation on the effect of the inflow angle, modulation Fourier-mode number, and its relative amplitude, as well as on their impact for three inlet-to-outlet radius ratios of the investigated diffuser.

(iii) Finally, we perform three-dimensional simulations in order to account for boundary layers developed on the parallel ring walls. The three-dimensional numerical simulations presented in this study are fundamentally different from those reported in our previous publications [30,31,33,34]. In the earlier work, the vast majority of our three-dimensional simulation results were obtained

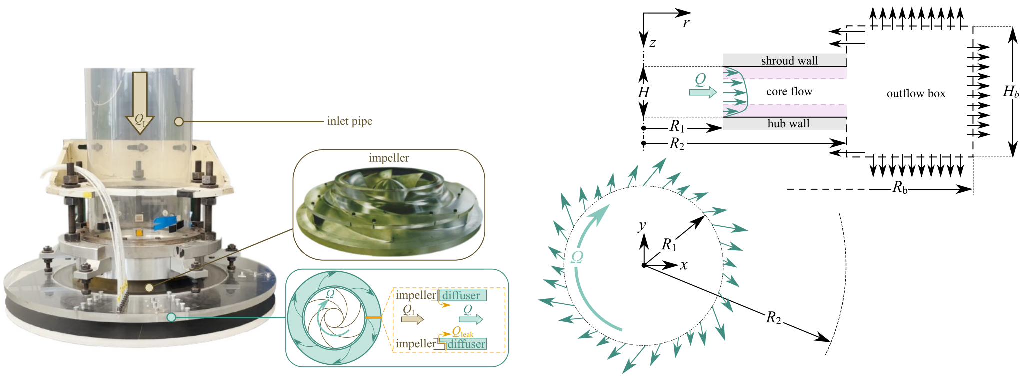

(a) Real system: Radial vaneless diffuser in a centrifugal pump

(b) Idealized system: Inlet-modulated radial swirling source flow

FIG. 1. (a) The radial vaneless diffuser of a centrifugal pump motivates the idealized system investigated in this study. (b) Schematic of the idealized system depicted in its longitudinal (top) and midplane (bottom) cross sections. The light-pink regions at the hub and shroud walls denote the boundary layer regions, while the light-blue arrows depict the inflow velocity, azimuthally modulated at the inlet and rotating with a rotation rate Ω, corresponding to the impeller rotation rate. The integral of the inlet velocity for the idealized configuration provides the volumetric flow rate Q (light-blue thick arrows), which accounts for the inlet pipe flow rate Q_I (brown arrows) and the leakage flow rate Q_{leak} between the impeller outlet and the diffuser inlet in the real system (orange arrows).

by simulating a whole centrifugal pump and focusing on its radial vaneless diffuser. This is similar to what is done in other investigations [16], where a rotating impeller imposes the inlet flow conditions of the vaneless diffuser (parallel annular plates). In contrast, the present study examines the fundamental flow in a canonical geometry in which the inlet boundary condition is precisely controlled through an inflow modulation strategy similar to the one employed in the preceding two-dimensional simulations [see Sec. II]. This simplified framework offers the advantage of providing clearer insights into the influence of inlet perturbations on the swirling radial source flow instability and will allow us to isolate the effects of the boundary layer in the destabilization budget of the canonical system we investigate.

The paper is therefore organized as follows: Section II introduces the problem and defines the mathematical framework. Section III outlines the discretization methods used to numerically solve the Navier–Stokes equations. Section IV presents the results of the linear stability analysis and nonlinear numerical simulations in two and three dimensions. Finally, Sec. V summarizes the findings and draws conclusions.

II. PROBLEM FORMULATION

A. Three-dimensional configuration

A schematic diagram of the three-dimensional problem configuration is depicted in Fig. 1(a). The considered system is composed of two parallel annular plates at constant axial distance H. The spatially modulated inlet is set at $r = R_1$ and rotates with a constant angular velocity Ω such that $\text{Re}_\Omega = \Omega R_1^2/\nu = 5.52 \times 10^5$ for all cases we consider hereinafter, where ν is the kinematic viscosity of the fluid and Re_Ω is a first Reynolds number scaled on the nominal tangential velocity at the inlet. A second Reynolds number is defined based on a volumetric flow rate Q entering the parallel annular plates, i.e., $\text{Re}_Q = Q/2\pi H\nu$. We employ a reference value $\widetilde{\text{Re}}_Q = \tilde{Q}/2\pi H\nu = 6.46 \times 10^4$ and vary the parameter $\Phi = \text{Re}_Q/\widetilde{\text{Re}}_Q = Q/\tilde{Q} \in [0.75,\ 1.25]$ to investigate the instabilities in the turbulent flow between parallel plates with radial aspect ratios $\Gamma = R_2/R_1 \in \{1.25, 1.5, 2\}$ and a cross-sectional aspect ratio $\Lambda = (R_2 - R_1)/H \in 515/154\{0.5, 1, 2\}$. These parameters are selected to match the values used in literature for carrying out numerical simulations [30–34] and experiments [7] in the complex configuration that inspired our simplified canonical flow.

Unsteady Reynolds-Averaged Navier–Stokes equations are employed such that the incompressible viscous flow between the two parallel annular plates is formulated by

$$\frac{\partial \boldsymbol{U}}{\partial t} + (\boldsymbol{U} \cdot \nabla)\boldsymbol{U} + \nabla P = \nabla \cdot (2\nu \boldsymbol{S} - \boldsymbol{\tau}), \quad \nabla \cdot \boldsymbol{U} = 0, \tag{1}$$

where $\boldsymbol{U}$ denotes the mean part of the velocity vector, P is the mean pressure field, $\boldsymbol{S} = \frac{1}{2}(\nabla \boldsymbol{U} + \nabla^T \boldsymbol{U})$ is the mean rate of the strain tensor, and $\boldsymbol{\tau}$ is the Reynolds stress tensor (see Refs. [35,36] for details).

The shear-stress transport (SST) k-ω turbulence model is employed for the Reynolds stress tensor, as it accounts for the transport of the principal turbulent shear stress. This characteristic makes the k-ω SST model more suitable for centrifugal flow simulations than both the standard and realizable k-ϵ models [30–34].

Other modifications to the standard k-ω SST model have been proposed in the literature [37] to include a cross-diffusion term in the ω equation and a blending function to ensure that the model equations behave appropriately in the near-wall and far-field zones [38]. In the present study, we employ one of such modified k-ω SST models, following the formulation of Menter [39]. The corresponding turbulent kinetic energy k equation is given by

$$\frac{\partial k}{\partial t} + (\boldsymbol{u} \cdot \nabla)k = P_k - \beta^* \omega k + \nabla \cdot [(\nu + \sigma_k \nu_T)\nabla k], \tag{2}$$

and for the turbulence-specific dissipation rate ω, it yields

$$\begin{aligned}\frac{\partial \omega}{\partial t} + (\boldsymbol{u} \cdot \nabla)\omega = {}& \alpha S^2 - \beta \omega^2 + \nabla \cdot [(\nu + \sigma_\omega \nu_T)\nabla \omega] \\ & + 2(1 - F_1)\frac{\sigma_{\omega 2}}{\omega} \nabla k \cdot \nabla \omega,\end{aligned} \tag{3}$$

where the production term P_k is given by

$$P_k = \nu_T \boldsymbol{S}(u) : \boldsymbol{S}(u), \tag{4}$$

and the blending function F_1 is defined by

$$F_1 = \tanh\left\{\left\{\min\left[\max\left(\frac{2\sqrt{k}}{\beta^* \omega y}, \frac{500\nu}{y^2 \omega}\right), \frac{4\rho \sigma_{\omega 2} k}{CD_{k\omega} y^2}\right]\right\}^4\right\}, \tag{5}$$

with $CD_{k\omega} = \max(2\rho\sigma_{\omega 2}\frac{1}{\omega}\nabla k \cdot \nabla \omega, 10^{-10})$, y being the normal distance to the nearest wall. Finally, the turbulent eddy viscosity ν_T is defined as

$$\nu_T = \frac{\alpha_1 k}{\max(\alpha_1 \omega, S F_2)}, \tag{6}$$

where F_2 is a second blending function:

$$F_2 = \tan\left[\left[\max\left(\frac{2\sqrt{k}}{\beta^* \omega y}, \frac{500\nu}{y^2 \omega}\right)\right]^2\right]. \tag{7}$$

Further details of the modeling techniques and the constants $(\beta, \beta^*, \sigma_k, \sigma_{\omega 2}, \alpha_\omega)$ of this model can be found in Menter's publication [39].

The azimuthally averaged diffuser inlet velocity profiles of the three velocity components [$\overline{U}_r(z)$, $\overline{U}_\theta(z)$, and $\overline{U}_z(z)$] at $r = R_1$ are modeled as explicit fitting functions resulting from our previous studies [32] and are here used to reproduce the mean inlet flow features that we aim to take into account to grant comparability with our previous experiments and simulations in which the targeted instability has been observed. Then, a modulated radial source structure perturbation is approximately mimicked by superposing a m_F-periodic Fourier mode in the circumferential direction:

$$U_r(\theta, z) = \overline{U}_r(z)\{1 + A\cos[m_F(\theta - \Omega t)]\}, \tag{8a}$$

$$U_\theta(\theta, z) = \overline{U}_\theta(z)\{1 + A\sin[m_F(\theta - \Omega t)]\}, \tag{8b}$$

$$U_z(\theta, z) = \overline{U}_z(z)\{1 + A\cos[m_F(\theta - \Omega t)]\}, \tag{8c}$$

where A denotes the amplitude of the Fourier mode and m_F is its wave number. The phase shift between radial and axial velocities [$\approx\cos[m_F(\theta\text{-}\Omega t)]$] compared with the tangential velocity [$\approx\sin[m_F(\theta\text{-}\Omega t)]$] is motivated by the single-Fourier-mode continuity equation in cylindrical coordinates. For fixed walls, the no-slip boundary condition is applied. The static pressure $P = 0$ Pa is set for an outflow box [see Fig. 1(b)] of height H_b and radius R_b attached to the diffuser outlet, where $H_b/H = 15$ and $R_b/R_2 = 3$.

The inlet value for the turbulent kinetic energy k_{in} is estimated by

$$k_{in} = \tfrac{3}{2}(I|u_{ref}|)^2, \tag{9}$$

where u_{ref} is the reference velocity, defined as the radial velocity at the inlet, and I denotes the turbulence intensity given by

$$I = 0.16(\mathrm{Re}_Q)^{-\frac{1}{8}}. \tag{10}$$

The turbulent specific dissipation rate at the inlet ω_{in} is calculated as

$$\omega_{in} = \frac{k_{in}^{0.5}}{C_\mu^{0.25} l}, \tag{11}$$

where C_μ is a constant with a value of 0.09, and l denotes a reference length scale, taken as the diffuser height in the present simulations. Along the walls, we impose

$$k_{wall} = 0, \quad \omega_{wall} = \frac{60\nu}{0.075} y_1^2, \tag{12}$$

where the subscript "wall" denotes the boundary condition of the turbulence model at the walls, and y_1 represents the distance from the center of the first cell to the nearest wall [40]; more details are described in Sec. III.

We finally stress that, although the k-ω SST model is frequently reported to outperform standard and realizable k-ε formulations in flows with adverse pressure gradients and separation, its reliability in strongly rotating or swirling flows remains limited and highly case-dependent [41,42]. More fundamentally, linear eddy-viscosity models based on the Boussinesq hypothesis are known to be structurally inadequate for rotating flows because they enforce an isotropic stress-strain relationship and therefore fail to represent the strong Reynolds-stress anisotropy, rotation-induced redistribution mechanisms, and centrifugal effects that dominate turbulence production and transport in such configurations [43]. Although rotation and curvature corrections have been proposed to alleviate some of these deficiencies [44], they do not remove the underlying closure limitation and cannot be expected to provide robust predictions across different rotating-flow regimes. We note that these well-known weaknesses will be addressed through a comparison between turbulent and inviscid simulations. If turbulence modeling is shown to have a significant impact on the flow instability, the in-depth analysis will be limited, and a detailed investigation will be deferred to future large-eddy simulations of the swirling source flow.

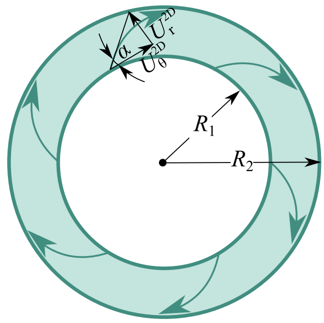

FIG. 2. Schematic of the two-dimensional core flow at the midheight of the diffuser, where the flow angle α is defined as the angle between the flow path and the tangential direction, i.e., $\alpha = \arctan(U_r^{2D}/U_\theta^{2D})$.

B. Two-dimensional simplified configuration

To study the core flow instability in the turbulent swirling radial source flow between parallel annular plates, the two-dimensional flow at the midheight of the parallel annular plates with finite radial aspect ratio Γ (as depicted in Fig. 2) is also considered. Based on the assumption that the core flow between the parallel annular plates is quasi two-dimensional, the effect of wall boundary layers is neglected in this configuration; we therefore compare the fully three-dimensional (3D) flow with a two-dimensional simplified configuration. For the inflow boundary condition, the mean tangential velocity is specified referring to the 3D full pump simulation results as $\overline{U}_\theta^{2D} = 0.655\Omega R_1$, and the mean radial velocity is specified as $\overline{U}_r^{2D} = Q/2\pi R_1 H$ corresponding to a preset value of the inlet flow rate Q. We therefore stress that the velocity triangle depicted in Fig. 2 provides the link between the nondimensional parameter Φ (determined via the flow rate Q) and the inflow angle α. The modulated radial source structure perturbation is approximately mimicked by superposing an m-periodic Fourier mode:

$$U_r^{2D}(\theta) = \overline{U}_r^{2D}\{1 + A\cos[m_F(\theta - \Omega t)]\}, \tag{13a}$$

$$U_\theta^{2D}(\theta) = \overline{U}_\theta^{2D}\{1 + A\sin[m_F(\theta - \Omega t)]\}. \tag{13b}$$

For the outlet, we set the static pressure $p = 0$ Pa, and zero gradient for the velocity field.

C. Logarithmic spiral flows configuration

Under the hypothesis of a two-dimensional core flow mechanism for the instability, a two-dimensional linear stability analysis will be performed using the analytical model of Tsujimoto *et al.* [19]. This model has successfully predicted the Fourier-mode-3 instability observed in a previous study of Heng *et al.* [22,29], and it will further help to clarify the origin of the rotating instability at low flow rates. We recall that several assumptions are made in the model of Tsujimoto *et al.* [19] because the flow is two-dimensional, incompressible, and inviscid; the boundary conditions are rotationally symmetric; uniform static pressure at the diffuser outlet and imposed velocity magnitude and flow angle at the inlet; the flow is described as a steady basic state that only depends on the radial coordinate.

Under these assumptions, the basic state streamlines in the vaneless diffuser take the form of logarithmic spirals extending from the diffuser inlet to the outlet. By utilizing scaling factors for length, time, velocity, and pressure, denoted as R_1, $(2\pi R_1^2)/Q$, $Q/2\pi R_1$, and $\rho Q^2/(2\pi R_1)^2$, respectively, the velocity $\boldsymbol{U}_0 = (U_{0,r}, U_{0,\theta})$ and pressure of the basic state are

$$U_{0,r} = \frac{1}{r}, \quad U_{0,\theta} = \frac{\mu}{r}, \quad P_0 = -\frac{1}{2}(1+\mu^2)\left(\frac{1}{r^2} + \frac{1}{\Gamma^2}\right), \tag{14}$$

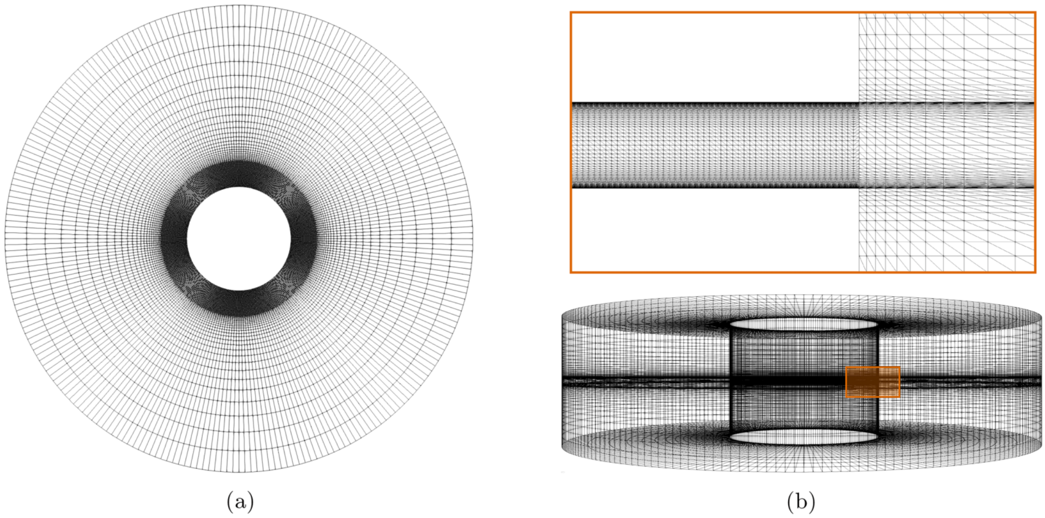

FIG. 3. (a) Top and (b) side view of a typical mesh employed for carrying out the three-dimensional URANS numerical simulations in OpenFOAM. The inset in panel (b) shows a close-up (orange) of the refined grid in the radial diffuser.

where $\mu = U_{0,\theta}/U_{0,r}|_{r=1}$ and $1 < r < \Gamma$. We further remark that such a basic state is irrotational, i.e., $\nabla \times \boldsymbol{U}_0 = 0$. In the linear stability analysis, the total flow is expressed as the superposition of the basic state and the infinitesimal perturbation (denoted by a prime):

$$\begin{aligned} U_r &= U_{0,r}(r) + u'_r(r,\theta,t), \\ U_\theta &= U_{0,\theta}(r) + u'_\theta(r,\theta,t), \\ P &= P_0(r) + p'(r,\theta,t), \end{aligned} \tag{15}$$

where $\boldsymbol{U}' \ll \boldsymbol{U}_0$ and $p' \ll P_0$. Since the basic state is steady and homogeneous in the θ direction, the ansatz for the infinitesimal perturbation is given by

$$\{u'_r, u'_\theta, p'\} = \{\tilde{u}_r, \tilde{u}_\theta, \tilde{p}\}e^{i\xi t - im\theta}, \tag{16}$$

where m is the wave number for the perturbation, and $\{\tilde{u}_r, \tilde{u}_\theta, \tilde{p}\}$ are functions of the r only. The complex frequency ξ can be expressed as a combination of a real χ and an imaginary σ part, i.e., $\xi = \chi - i\sigma$. The real part χ represents the angular frequency, while σ corresponds to the instability growth rate. The flow is considered unstable when $\sigma > 0$ and stable when $\sigma < 0$. The mathematical problem is closed by applying the boundary conditions proposed by Tsujimoto *et al.* [19]:

$$r = 1\colon \tilde{u}_r = \tilde{u}_\theta = 0, \quad r = \Gamma\colon \tilde{p} = 0. \tag{17}$$

By fixing m and setting $\sigma = 0$, the neutral stability modes are determined following the algorithm proposed by Heng *et al.* [22], which employs a shooting method to iteratively approach the solution.

III. NUMERICAL METHOD

A high-quality mesh with sufficient cells and well-distributed nodes is essential to ensure the reliability of the simulation. In this study, a hexahedral mesh is employed (see Fig. 3) since it is generally cost-effective and less diffusive than a tetrahedral mesh, particularly in the boundary-layer region. Following a grid-independence analysis, a total of 2.3 million finite-volume cells was selected for the entire centrifugal machine simulation in our previous studies [32]. In this study, the grid number in the computational domain remains the same as in the previous studies, and the mesh

TABLE I. Boundary condition types used in OPENFOAM v1912.

Boundary surface	p	U	k	ω
Inlet	`zeroGradient`	`flowRateInletVelocity`	`fixedValue`	`fixedValue`
Outlet	`fixedValue`	`inletOutlet`	`inletOutlet`	`inletOutlet`
Interfaces	`cyclicAMI`	`cyclicAMI`	`cyclicAMI`	`cyclicAMI`
Fixed walls	`zeroGradient`	`noSlip`	`fixedValue`	`omegaWallFunction`

is refined near the walls, with an expansion ratio of 1.5, ensuring $y^+ \approx 1$. The Menter k-ω SST turbulence model we employed offers accurate near-wall handling, automatically adapting between low-Re formulations and wall functions according to the grid density [37,45].

To solve the proposed mathematical problem, we employ the open-source package OPENFOAM. Further information on the solvers we selected is reported in our earlier work [32]. Boundary treatment involves Dirichlet, Neumann, or mixed conditions. The OPENFOAM routine used to specify the inlet conditions is termed `codedFixedValue`. This boundary condition is implemented using user-defined code, which allows for more flexibility and customization compared with other built-in boundary conditions. For the outlet, we employed the `inletOutlet` routine, which applies a zero-gradient Neumann condition for outward flow, while inward flow is governed by a Dirichlet condition obtained through bulk extrapolation [46]. Distinct mesh zones (i.e., the fluid between the parallel annular plates and within the outflow box) are coupled employing the `cyclicAMI` routine at the mesh interfaces. Table I summarizes an overview of the OPENFOAM routines employed for modeling the boundary conditions in this study.

To balance numerical accuracy and computational efficiency, the simulation time step Δt was set to correspond to $\Delta\theta = 0.5^\circ$ of the runner rotation, i.e.,

$$\Delta t = \frac{\Delta\theta}{\Omega}\frac{\pi}{180^\circ}. \tag{18}$$

This choice is consistent with several studies in the literature [5], which recommend $\Delta\theta \leqslant 1^\circ$. The adopted time step yields a characteristic Courant number of

$$C = |U|\frac{\Delta t}{\Delta x} \approx 0.05, \tag{19}$$

where Δx denotes the local mesh size. The characteristic Courant number was evaluated for cells in the bulk region of the diffuser, representing the primary area of interest, employing the theoretical inlet velocity and a length scale derived from the mesh element volume. Subsequent *a posteriori* analysis confirmed that the domain-averaged Courant number across all simulations is $\overline{C} = 0.0075$ at the nominal flow rate.

IV. RESULTS

The instabilities within our swirling radial source flow with a given spatially modulated inlet are studied by increasing the complexity of the basic state. Our objective is to distinguish the contributions to instabilities from the mean flow and the inlet modulation, as well as evaluate the robustness of the core-flow mechanism to three-dimensional effects. We first employ linear stability analysis to identify the stability boundaries for the inviscid core-flow [Tsujimoto's model [19], see Eqs. (14)] and the mechanisms driving its destabilization. Subsequently, we perform two-dimensional numerical simulations incorporating inlet modulations without three-dimensional effects to investigate the impact of the inlet modulation as well as viscous dissipation and turbulent kinetic energy. Finally, three-dimensional simulations are conducted to examine the impact of the three-dimensional boundary layer effect at the top and bottom walls.

A. Two-dimensional LSA of the one-dimensional steady basic state

The linear stability analysis of the core swirling flow between parallel annular plates with different radius ratios Γ, i.e., $\Gamma \in \{1.25, 1.5, 2\}$, is first carried out for varying inflow angles α. Note that the definition of the inflow angle α here is the angle between the flow trajectory and the azimuthal direction at the inlet, i.e., $\alpha = \arctan(\mu)$. Neutral stability conditions (α_n) are associated with corresponding propagation velocity $\omega_{\rm n}$ predicted for different neutral stability modes, as depicted in the top panels of Fig. 4. The results demonstrate that the critical flow angle $\alpha_{\rm c}$, defined as the largest neutral inflow angle, i.e., $\alpha_c = \max(\alpha_n)$, leading to the onset of rotating instability, is approximately 6°, 10°, and 16° for $\Gamma = 1.25$, 1.5, and 2, respectively. This plot also shows that the most unstable Fourier mode varies with Γ, i.e., $m = 9$ for $\Gamma = 1.25$, $m = 5$ for $\Gamma = 1.5$, and $m = 4$ for $\Gamma = 2$. The neutrally stable basic state and the corresponding most dangerous Fourier mode for $\Gamma = 1.25$, 1.5, and 2 are shown in the middle and bottom panels of Fig. 4, respectively. The space-filling perturbation demonstrates the global nature of the instability that maximizes pressure disturbance p' near the diffuser inlet. The velocity perturbation magnitude $|\boldsymbol{U}'|$ is rather maximized at the diffuser outlet, where backflow cells are amplified by the linear inviscid instability.

To investigate the underlying physical mechanisms contributing to the flow instabilities and to verify the overall energy conservation of the neutral Fourier modes, we here conducted *a posteriori* a study of the kinetic energy transferred between the base state and the critical Fourier mode. For this purpose, all terms of the inviscid Reynolds–Orr equation are evaluated:

$$\frac{dE^{\rm kin}}{dt} = \sum_{k=1}^{4} \int_V I'_k dV + K^{\rm out}, \tag{20}$$

where $E^{\rm kin}$ denotes the total kinetic energy, while I'_k represents the kinetic-energy densities arising from the nonlinear term of the incompressible Euler equations,

$$K^{\rm out} = -\frac{1}{2} \int_{S^{\rm out}} U_{0,r}[(u'_r)^2 + (u'_\theta)^2] dS, \tag{21}$$

corresponds to the transport of perturbation energy across the outlet surface $S^{\rm out}$. Given that $\tilde{u} = 0$ at the inlet, perturbation energy is not introduced from upstream. Furthermore, the pressure forces do not contribute to the energy budget because pressure perturbations are assumed to vanish at the outlet (i.e., $\tilde{p} = 0$ at $r = \Gamma$). For clarity in interpreting the energy budget, the local energy production rates are decomposed along the base-state streamline coordinates,

$$\boldsymbol{U}' = \boldsymbol{U}'_\parallel + \boldsymbol{U}'_\perp, \tag{22}$$

here $\boldsymbol{U}'_\parallel$ denotes the perturbation component projected along the basic state streamlines, and $\boldsymbol{U}'_\perp = \boldsymbol{U}' - \boldsymbol{U}'_\parallel$ represents the component normal to the streamlines. The associated energy density terms I'_k are expressed by

$$\begin{aligned}\sum_{k=1}^{4} I'_k = -[&\boldsymbol{U}'_\perp \cdot (\boldsymbol{U}'_\perp \cdot \nabla \boldsymbol{U}_0) + \boldsymbol{U}'_\parallel \cdot (\boldsymbol{U}'_\perp \cdot \nabla \boldsymbol{U}_0) \\ &+ \boldsymbol{U}'_\perp \cdot (\boldsymbol{U}'_\parallel \cdot \nabla \boldsymbol{U}_0) + \boldsymbol{U}'_\parallel \cdot (\boldsymbol{U}'_\parallel \cdot \nabla \boldsymbol{U}_0)],\end{aligned} \tag{23}$$

here the index k enumerates all terms consecutively on the right-hand side of the equation. The local energy transfer associated with each integrand I'_k is classified as destabilizing (positive) or stabilizing (negative) depending on its sign. The term I'_1 corresponds to the amplification of the cross-stream perturbation velocity $\boldsymbol{U}'_\perp$ through transport of basic-state momentum $\boldsymbol{U}_0$ in the cross-stream direction. The terms I'_2 and I'_3 combine the streamline-perpendicular $\boldsymbol{U}'_\perp$ and streamline-parallel $\boldsymbol{U}'_\parallel$ perturbation velocities. In particular, I'_2 corresponds to the amplification of the parallel-stream perturbation velocity $\boldsymbol{U}'_\parallel$ through the transport of basic-state momentum $\boldsymbol{U}_0$ in the cross-stream direction $\boldsymbol{U}'_\perp \cdot \nabla \boldsymbol{U}_0$. In the present flow, this term is symmetric with I'_3, which represents the

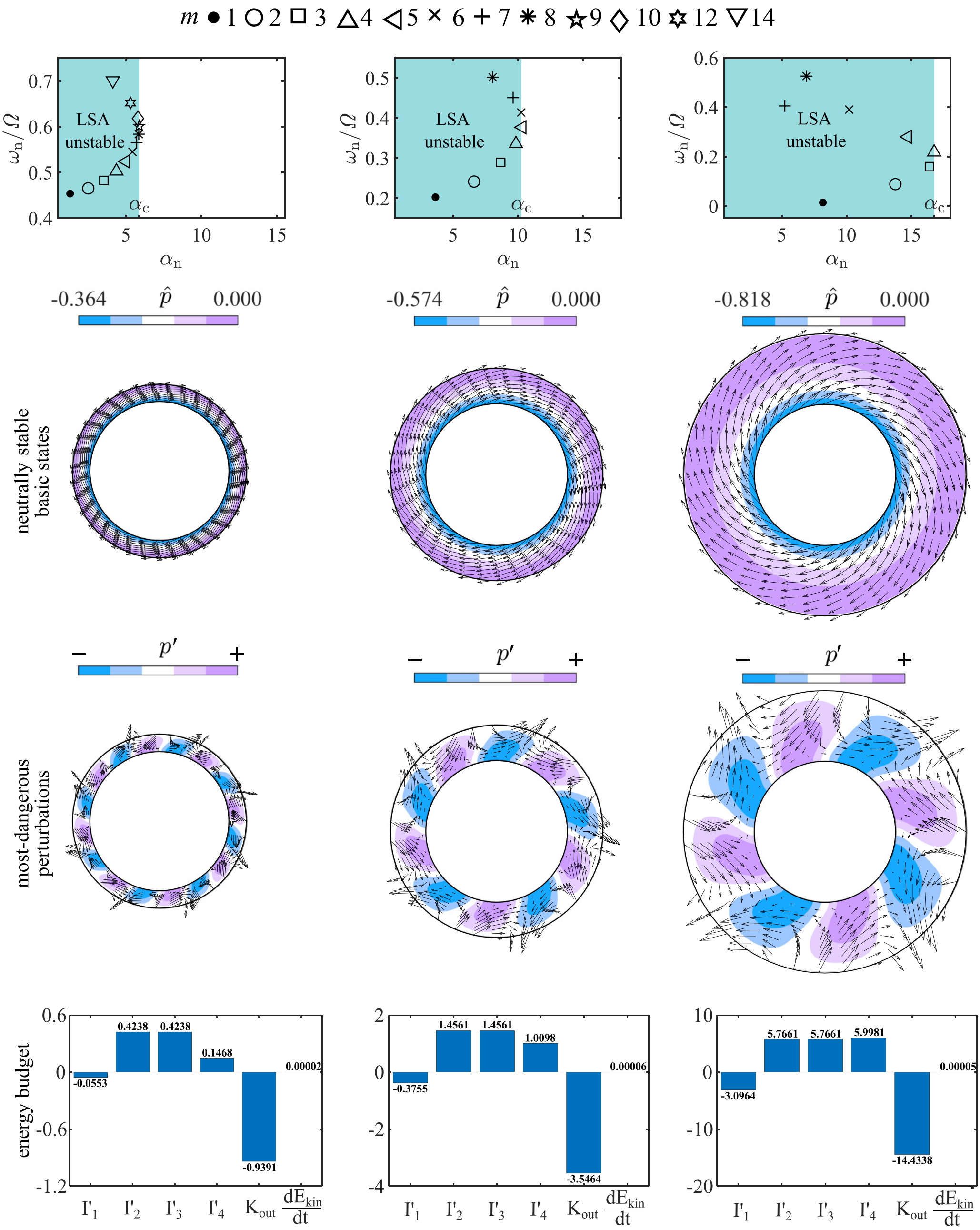

FIG. 4. (top) Critical flow angle and propagation velocity for different neutral Fourier modes. (upper middle) neutrally stable basic state depicted in terms of pressure (contours) and velocity (arrows). (lower middle) Most-dangerous perturbation for the pressure (contours) and the velocity (arrows) fields. (bottom) energy budget for the most dangerous perturbation. Three radius ratios are considered: $\Gamma = 1.25$ (left), $\Gamma = 1.50$ (center), $\Gamma = 2$ (right).

amplification of the cross-stream perturbation velocity $\boldsymbol{U}'_\perp$ through the transport of basic-state momentum $\boldsymbol{U}_0$ in the parallel-stream direction $\boldsymbol{U}'_\parallel \cdot \nabla \boldsymbol{U}_0$. Finally, the term I'_4 is connected to flow decelerations along the basic state streamlines because it describes the amplification of the parallel-stream perturbation velocity $\boldsymbol{U}'_\parallel$ through the transport of basic-state momentum $\boldsymbol{U}_0$ in the parallel-stream direction. A decrease in the basic-state momentum (deceleration) results in a positive contribution of $I'_4 = -\boldsymbol{U}'_\parallel \cdot (\boldsymbol{U}'_\parallel \cdot \nabla \boldsymbol{U}_0)$, thereby inducing an energy transfer from the basic state to the perturbation.

A positive kinetic-energy rate of change $d_t E^{\text{kin}}$ indicates unstable of the basic flow. Consequently, the energy budget serves to validate the linear stability results, since it must be zero for neutral Fourier modes, which means that

$$\frac{dE^{\text{kin}}}{dt}|_{\sigma=0} = 0. \tag{24}$$

Our computations meet this condition at the fifth significant digit, thereby ensuring the validation of the neutral Fourier mode.

To supplement the qualitative analysis conducted so far based on the scalar fields of I'_k, the total energy budget is also reported in Fig. 4 for $\Gamma = 1.25$ (left), 1.50 (middle), and 2.00 (right) for the most dangerous perturbations. Our results show that, for the three different radius ratios Γ with different instability Fourier modes, the instability mechanism is similar, $\int_V I'_2 dV$, $\int_V I'_3 dV$, and $\int_V I'_4 dV$ consistently destabilize the basic state. On the other hand, $\int_V I'_1 dV$ has a minor stabilizing effect, while most of the energy produced by $\int_V I'_2 dV$, $\int_V I'_3 dV$, and $\int_V I'_4 dV$ is transported outside of the diffuser, leading to a high-magnitude, negative K^{out}. Thus, the instability of the diffuser basic state arises from two contributing mechanisms:

(1) The lift-up and reverse lift-up mechanisms, associated with I'_2 and I'_3, respectively, are facilitated by the logarithmic-spiral geometry of the basic-state streamlines, whereby fluid elements displaced in the cross-stream direction encounter different basic-state velocities, hence effective mean shear.

(2) The streamwise deceleration results from the radial expansion of the diffuser cross-section, hence from the purely radial adverse pressure gradient. As the basic state streamlines are logarithmic spirals, a part of the radial basic state pressure gradient will be projected onto the basic state streamlines, leading to an effective flow deceleration that increases with Γ. Such a streamwise deceleration represents a crucial destabilizing mechanism in all radial source flows.

We further stress that a great advantage of using Tsujimoto's model to investigate the instability in a vaneless diffuser allows us to exclude two potential origins for the flow instability:

(i) Because Tsujimoto's model assumes a uniform, steady flow in θ and does not explicitly identify Coriolis effects as the driving mechanism, we conclude that the observed instabilities are unlikely to be primarily governed by Coriolis destabilization mechanisms.

(ii) In principle, the lift-up and reverse lift-up mechanisms can lead to centrifugal instabilities. We therefore apply the criterion proposed by Ref. [47], which provides a necessary condition for the occurrence of centrifugal instabilities in inviscid, incompressible, two-dimensional planar flows in rotating systems. This criterion generalizes the classical Rayleigh criterion by introducing the local algebraic radius of curvature $\ddot{R}$ of the basic-state streamlines, evaluated at each point along the flow:

$$\ddot{R} = \frac{|\boldsymbol{U}_0|^3}{(\nabla \psi_0) \cdot [\boldsymbol{U}_0 \cdot \nabla \boldsymbol{U}_0]}, \tag{25}$$

where ψ_0 is the basic state stream function. The criterion of [47] is formulated in terms of the following quantity:

$$\delta = 2\left(\frac{|\boldsymbol{U}_0|}{\ddot{R}} + \hat{\Omega}\right)(\nabla \times \boldsymbol{U}_0 + 2\hat{\Omega}), \tag{26}$$

where $\hat{\Omega}$ denotes the rotation rate of the coordinate system. As the model of Tsujimoto is steady in a nonrotating reference frame, $\hat{\Omega} = 0$. According to Ref. [47], the flow can be unstable to centrifugal instability if there exists a streamline ψ_0 such that $\max_{\psi_0}(\delta) < 0$. Rewriting our steady base flow, the terms entering the local algebraic radius of curvature can be computed as

$$U_{0,r} = \frac{1}{r}\frac{\partial \psi_0}{\partial \theta}, \quad U_{0,\theta} = -\frac{\partial \psi_0}{\partial r}, \tag{27}$$

which yields

$$\nabla \psi_0 = \begin{bmatrix} \dfrac{\partial \psi_0}{\partial r} & \dfrac{1}{r}\dfrac{\partial \psi_0}{\partial \theta} \end{bmatrix} = [-U_{0,\theta} \quad U_{0,r}] = \begin{bmatrix} -\dfrac{\mu}{r} & \dfrac{1}{r} \end{bmatrix}, \tag{28}$$

and we can calculate

$$(\nabla \psi_0) \cdot [\boldsymbol{U}_0 \cdot \nabla \boldsymbol{U}_0] = \frac{\mu}{r^4}(1 + \mu^2). \tag{29}$$

Considering that $|\boldsymbol{U}_0|^3 = \frac{1}{r^3}(\mu^2 + 1)^{\frac{3}{2}}$, the radius of curvature of the basic state streamlines is

$$\ddot{R} = \frac{r}{\mu}\sqrt{\mu^2 + 1}. \tag{30}$$

Hence, the final expression for δ reads

$$\delta = \frac{2\mu \nabla \times \boldsymbol{U}_0}{r^2}. \tag{31}$$

Since the basic state is irrotational, i.e., $\nabla \times \boldsymbol{U}_0 = 0$, the flow is therefore neutrally stable with respect to centrifugal instability. Consequently, the necessary condition for attributing the observed instability to a Rayleigh-type centrifugal mechanism is not satisfied under the simplifying assumptions of the model of Ref. [19]. The instability identified in the present study is thus not of centrifugal origin.

For $\Gamma = 1.25$, $\int_V I_4' dV$ is always lower in magnitude compared with $\int_V I_2' dV$ and $\int_V I_3' dV$. This is expected because the diffuser is short in the radial direction; hence, the corresponding streamwise deceleration makes a minor contribution to destabilization. For $\Gamma = 1.50$, with the instability Fourier-mode number $m \leqslant 3$, $\int_V I_4' dV$ being slightly dominant in magnitude, the streamwise deceleration becomes stronger. As m increases above 3, the lift-up mechanism plays a more important role in the destabilization. For $\Gamma = 2$, the streamwise deceleration mechanism is the dominant mechanism except for $m = 5$ and $m = 6$, which are, however, far from being critical.

Based on the understanding of the destabilization mechanisms, we expect that azimuthal modulation plays a significant role if Γ is small, such that shear-induced mechanisms provide the most dangerous perturbation with the largest energy amplification. As for $\Gamma = 2$, deceleration is dominant, and it does not rely on a shear layer. Hence, from the LSA of the core flow, we can expect that no major instabilities are associated with the spatial modulation on $\alpha_c(\Gamma = 2)$.

B. Two-dimensional URANS simulation

The linear stability analysis employed in Sec. IV A did not account for nonlinear interactions between perturbation Fourier modes and the basic state. Even though it has been validated for its ability to predict the instability Fourier mode observed in the experiment of this diffuser for $\Gamma = 1.5$ (see Fan *et al.* [33]), the linear approach is clearly limited to predicting the asymptotic stability of each standalone perturbation Fourier mode. Moreover, the linear approach based on the model of Tsujimoto *et al.* [19] relies solely on the skewness of the diffuser inflow without incorporating any inhomogeneous forcing in the θ direction. Hence, we carried out a parametric study of around 500 two-dimensional numerical simulations that consider the nonlinearities and the inflow modulation in θ direction, and they also include viscous effects and turbulence modeling. We further recall that

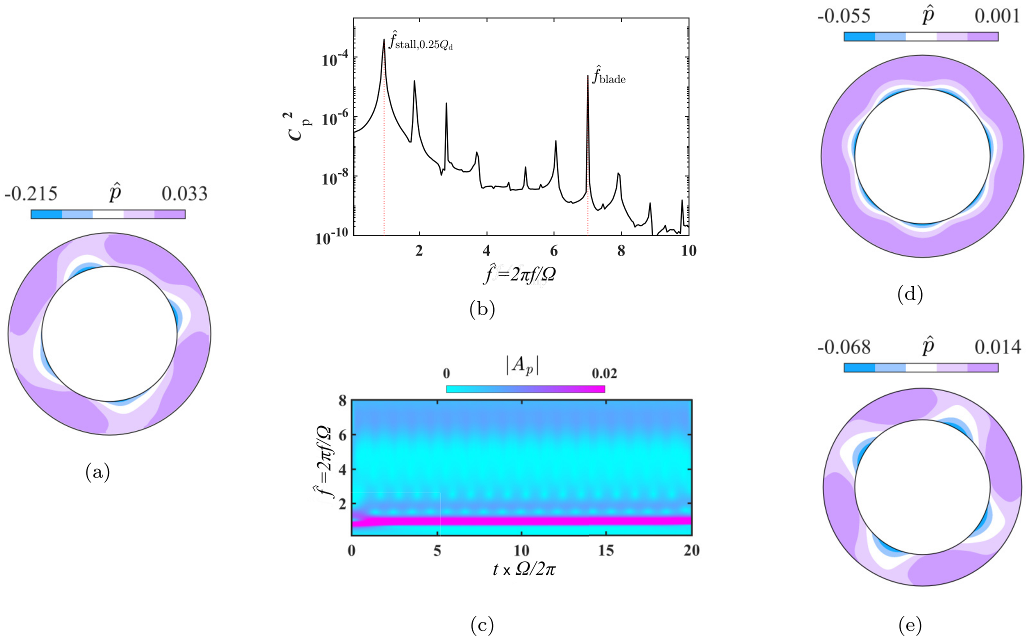

FIG. 5. Two-dimensional URANS simulation results for $\Gamma = 1.50$ at $\Phi = 0.25$ with a seven-periodic inflow Fourier mode $m_F = 7$ with an amplitude $A = 0.35$: (a) Instantaneous static pressure field; (b) Fourier analysis results; (c) Wavelet analysis results; (d) Phase-averaged static pressure field in a reference frame rotating with the inflow radial source flow modulation; (e) Phase-averaged static pressure field in a reference frame rotating with the identified instability Fourier mode.

the inflow-modulated radial swirling source structure perturbation is approximately mimicked by superposing a m_F-periodic Fourier mode with different amplitude A in the circumferential direction [see Eqs. (13)].

Our goal is to identify a rotating instability in a basic state with a rotating inlet radial source flow modulation. This is significantly more complex than extracting the most dangerous Fourier mode from the previous LSA computations. In this study, we identify the propagation pattern of the instability by employing the cross-power spectra analysis of two numerical probes placed at the midradial distance of the diffuser with an angular phase shift of 60° [48,49]. The frequency f_{inst} and propagation velocity ω_{inst} of the unstable Fourier modes can be identified by performing fast Fourier transform (FFT) and cross-correlation analyses on the signals from the two probes. In addition, wavelet analysis was performed to capture the temporal evolution of the unstable Fourier modes, addressing the limitations of FFT in handling unsteady signals. Such instability characteristics are further confirmed by visualizing the flow fields. As an example, the simulation result for the diffuser radius ratio $\Gamma = 1.50$ with a seven-periodic inflow Fourier mode with an amplitude $A = 0.35$ at the inflow angle $\alpha = 2.50^\circ$ (corresponds to the flow rate ratio $\Phi = 0.25$) is depicted in Fig. 5. For this case, by visualizing the instantaneous flow field, we can observe a Fourier-mode-4 instability. By performing FFT and wavelet analyses [see Figs. 5(b) and 5(c)], we identify the inlet Fourier-mode frequency as $2\pi \hat{f}_{\mathrm{inlet}}/\Omega = 7$ and the instability frequency as $2\pi \hat{f}_{\mathrm{inst}}/\Omega = 0.75$, which corresponds to the four-periodic instability pattern rotating at $\omega_{\mathrm{inst}}/\Omega = 0.1875$. By phase-averaging the static pressure field in a reference frame rotating with the inlet radial source flow modulation, a uniform flow field can be observed [see Fig. 5(d)]. Such a primary phase-averaged flow field is approximately the basic state of the flow. By subtracting the primary phase-averaged result from the instantaneous pressure fields and performing a second phase average in a reference frame rotating with the

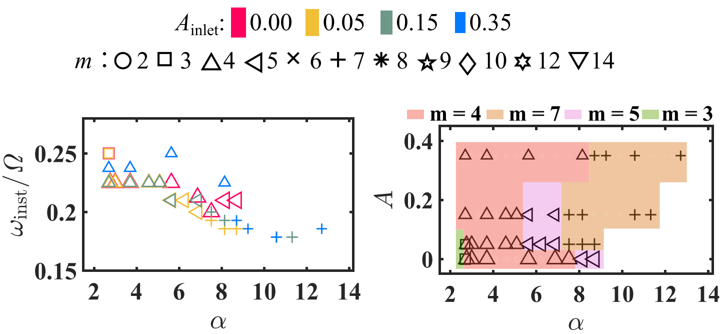

FIG. 6. Instability characteristic diagram of the flow in the diffuser of radius ratio $\Gamma = 1.50$ with a seven-periodic inflow Fourier mode with four different amplitudes A.

frequency $\omega_{\rm inst}$, the slow periodic rotating instability pattern is identified as shown in Fig. 5(e). A consistent postprocessing approach is employed for all other cases investigated in this study.

Our study employs a single $m_{\rm F}$-periodic Fourier mode to model the inlet radial source flow modulation. The Fourier mode is set to perturb both $U_{\rm r}$ and U_θ at the diffuser inlet with cosine and sine functions, respectively. Note that some differences exist between the inlet radial source flow modulation in our two-dimensional URANS simulation and that reported in the previous study by Ljevar *et al.* [20]. The impacts of these inflow differences on the flow characteristics are evaluated in detail in Appendix A.

For the URANS simulation with mean inflow ($A = 0$), the basic state is qualitatively the same as the LSA model. With the increase of the inflow Fourier-mode amplitude, the basic state is gradually characterized by the seven-periodic inflow modulations (see Fig. 19 in Appendix C). The protocol for the two-dimensional URANS parametric study is as follows:

(1) conduct numerical simulations by decreasing the flow rate Φ from 1.25 to 0.25 under a seven-periodic inflow Fourier perturbation, with the amplitude A increasing from 0 to 0.35, and varying the inflow Fourier mode number ($m_{\rm F} = 7, 5, 3$) and the diffuser radius ratio ($\Gamma = 1.25, 1.5, 2$).

(2) perform statistically stable FFT analysis on all simulation results and further confirm the flow field characteristics through flow visualization.

(3) summarize the instability characteristics, comprising the quantity and the propagation velocity of stall cells, using tables for comparative analysis.

(4) apply phase averaging to the numerical results at key operating points to better capture the structure of unstable Fourier modes and deepen the understanding of the instability mechanisms.

1. Instability characteristics of the reference case ($m_{\rm F} = 7$, $\Gamma = 1.5$)

Concerning the simulation result with the seven-periodic inflow Fourier mode, the instability Fourier-mode diagram (right panel of Fig. 6) shows the dominant instability Fourier-mode number with homogeneous inflow ($A = 0$) at the inflow angle $\alpha = 2.69^\circ$ (corresponding to the flow rate ratio $\Phi = 0.25$) is $m = 3$. As the flow angle α increases, the dominant instability Fourier-mode number changes to $m = 4$ with the inflow angle $2.69^\circ < \alpha < 8.14^\circ$ (corresponds to the flow rate ratio $0.25 < \Phi < 0.625$). The Fourier-mode-5 instability is dominant when the inflow angle $\alpha > 8.14^\circ$ (corresponds to the flow rate ratio $\Phi > 0.625$). To visualize the leading instability patterns, a phase average is applied to the last 120 time steps of the URANS simulation results. The top panel of Fig. 7 shows an overview of the instability scenario for the two-dimensional swirling radial source flow with a homogeneous inlet for four different inflow angles $\alpha \in \{2.69^\circ, 3.69^\circ, 5.63^\circ, 8.14^\circ\}$.

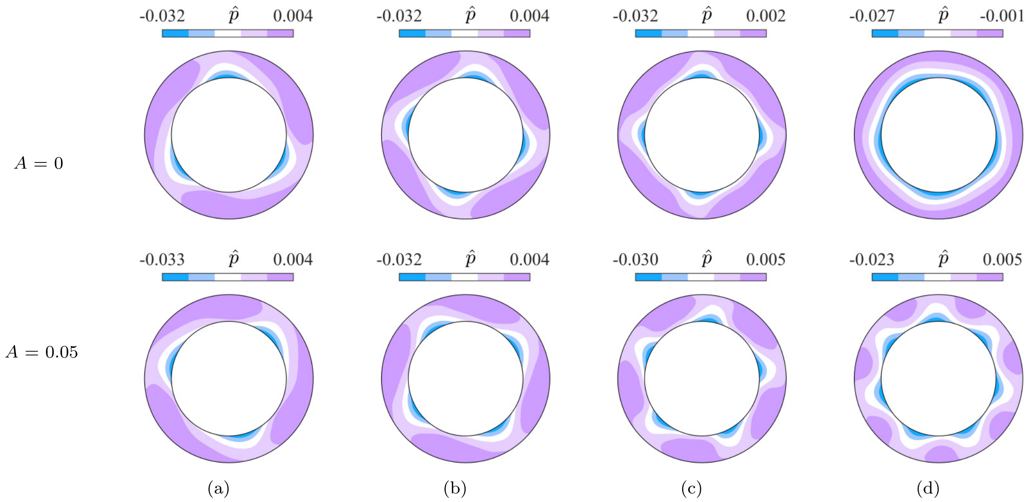

FIG. 7. Phase-averaged static pressure field for the diffuser of radius ratio $\Gamma = 1.50$ with a homogeneous inflow (top panel) and a seven-periodic inflow Fourier mode $m_{\mathrm{F}} = 7$ with an amplitude $A = 0.05$ (bottom panel) in a reference frame rotate in a reference frame rotate with the identified instability Fourier mode under different flow angles: (a) $\alpha = 2.69^{\circ}$ ($\Phi = 0.25$), (b) $\alpha = 3.69^{\circ}$ ($\Phi = 0.375$), (c) $\alpha = 5.63^{\circ}$ ($\Phi = 0.5$), and (d) $\alpha = 8.14^{\circ}$ ($\Phi = 0.625$).

As seven-periodic Fourier modes with different amplitudes A are applied to the inflow, the linearly unstable Fourier-mode-4 and -5 instabilities remain dominant for lower flow angles ($\alpha < 7.52^{\circ}$). However, for larger flow angles ($\alpha \geqslant 7.52^{\circ}$), the Fourier-mode-7 instability is dominant and becomes the critical Fourier mode. This conclusion is further confirmed by the phase-averaged flow fields as depicted in Fig. 7. Besides, with the increment of the amplitude A of the inflow Fourier mode, such instability occurs for higher flow angles α. We note that the inflow Fourier mode m_{F} selects the Fourier-mode number $m = 7$, which is already linearly unstable [see Fig. 4(b)]. It is therefore plausible to speculate that the flow destabilization still relies on linear mechanisms (see Sec. IV A) of the mean core flow, and the inlet modulation solely picks the most dangerous perturbation to trigger. Hence, this instability does not belong to the radial swirling source flow modulation instability as speculated by Ljevar *et al.* [20].

To more accurately quantify the impact of the inlet radial source flow modulation on instability characteristics, we perform an energy budget analysis on the URANS simulation results using the same methodology outlined in Sec. IV A. We consider the phase-averaged flow fields in the two reference frames as the basic state and perturbation, respectively. The comparison of calculated energy production terms of the Reynolds–Orr equation of phase-averaged models with a mean inlet ($A = 0$) and weakest inlet swirling modulation ($A = 0.05$) at the neutral stable condition ($\alpha = 8.70^{\circ}$) reveals only I_2' and I_4' terms have significant changes, with $\Delta I_1' \approx 0.14$ and $\Delta I_4' \approx=$ -0.15 upon an increase of A. This explains why the inflow modulation can select the instability Fourier-mode numbers, as it leads to the energy transformation from the I_4' to I_2' term associated with the lift mechanism related to shear.

Concerning the identified instability propagation velocity [see the top panel of Fig. 16(a)], it is slightly affected by the magnitude of the inlet perturbation A while it correlates with the instability Fourier-mode number m because it is expected that m increased and ω_{inst} decreased. For the inflow angle α between 2.69° and 6.87°, the instability propagation velocity ω_{inst} remains almost unchanged, ranging from $\omega_{\mathrm{inst}} = 0.25\Omega$ for $m = 3$ to $\omega_{\mathrm{inst}} = 0.22\Omega$ for $m = 4$. As the inflow angle α increases above 6.87°, the instability propagation velocity ω_{inst} starts to decrease sublinearly.

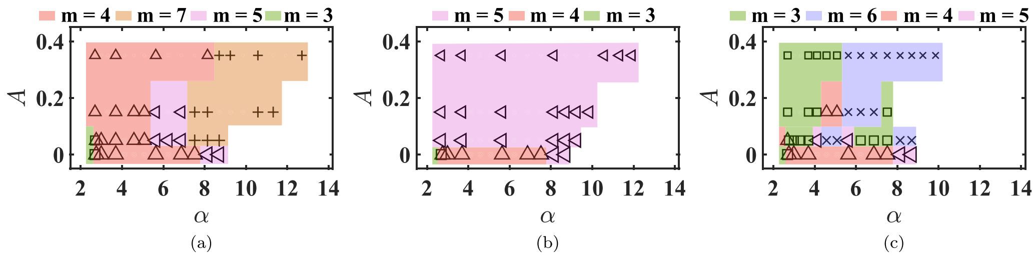

FIG. 8. Instability characteristic diagram of the flow in the diffuser of radius ratio $\Gamma = 1.50$ with a periodic inflow Fourier mode with four different amplitudes A and three different Fourier-mode numbers m_F: (a) $m_F = 7$, (b) $m_F = 5$, and (c) $m_F = 3$.

When the inflow angle α exceeds about 9.85°, the propagation velocity ω_{inst} saturates around 0.18 times the impeller rotational velocity Ω.

2. *Effect of inflow Fourier mode for* $\Gamma = 1.5$

Here we study the effect of the inflow Fourier mode, i.e., different Fourier-mode numbers and different amplitudes of the inflow perturbations, on the instability characteristics of the core flow between parallel annular plates.

The comparison of the phase-averaged instability Fourier modes resulting from inflow perturbations with three different Fourier-mode numbers, $m_F \in \{7, 5, 3\}$, all with a constant amplitude of $A = 0.05$ and subjected to varying inflow angles, is reported in Appendix D (see Fig. 21). Note that the basic states always look alike for all m_F considered and are therefore not shown. However, the instability Fourier modes reveal significant qualitative differences in the resulting pressure fields. While there are regions of the parametric space that can admit similarities among $m_F \in \{7, 5, 3\}$ [see Fig. 21(b) in Appendix D], notable differences are still observed, even with a constant amplitude of $A = 0.05$ [see Figs. 21(a) and 21(c) in Appendix D].

To have a more comprehensive parametric study for different amplitudes of the inflow Fourier mode, $A \in \{0, 0.05, 0.15, 0.35\}$ and different periodicity, $m_F \in \{7, 5, 3\}$, the comparison of the propagation velocity ω_{inst}, and the Fourier-mode diagram of the instability identified for the diffuser of radius ratio $\Gamma = 1.50$ are depicted in Fig. 8.

The simulation results with a seven-periodic inflow Fourier mode, i.e., for $m_F = 7$, were discussed in the previous section. We further recall that with homogeneous inflow ($A = 0$), the dominant instability Fourier-mode number changes from $m = 3$ to 4 to 5 owing to nonlinearities as the inflow angle α increases. For $m_F = 7$ with different amplitudes A applied to the inflow, the $m = 7$ instability is selected by the inflow Fourier mode for larger flow angles. As depicted in the top row of Fig. 21, the phase-averaged pressure field reveals the mode-4, mode-5, and mode-7 instability patterns under three different flow angles.

For the results with $m_F = 5$, the $m = 5$ instability is triggered as a dominant Fourier mode for all different inflow angles [see instability mode diagram in Fig. 8(b) and phase-averaged pressure field in the middle row of Fig. 21]. Here we recall the linear stability analysis result of the diffuser with radius ratio $\Gamma = 1.50$ [see Fig. 4(b)], the most unstable Fourier mode is $m = 5$, which is why the mode-5 instability is easily triggered by a five-periodic inflow Fourier mode ($m_F = 5$) with all different amplitudes at all different flow angles. Besides, the propagation velocity ω_{inst} decreases with the increase of the flow angle α and then maintains the same level after the flow angle α reaches about 8.70° [see Fig. 20(b) in Appendix D], which is similar to the results with a seven-periodic inflow Fourier mode [see $m_F = 7$ in Fig. 8(a)].

Regarding the result with a three-periodic inflow Fourier mode [see $m_F = 3$ in Fig. 8(c)], a $m = 3$ instability is triggered for lower flow angles. In addition, a Fourier-mode-6 instability occurred at higher flow angles due to the superharmonic of the inflow Fourier mode. This result is also in very

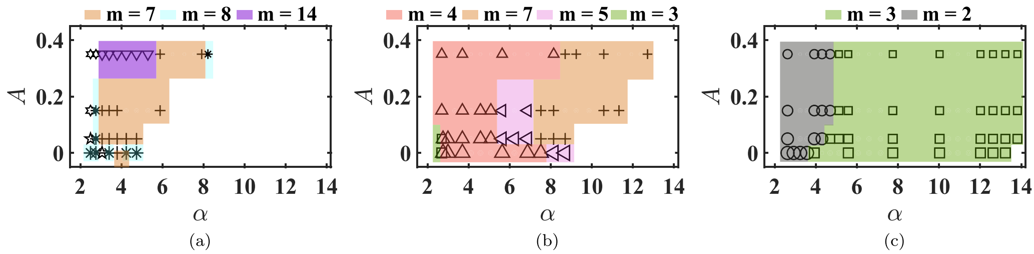

FIG. 9. Instability characteristic diagram of the flow in the diffuser with a seven-periodic inflow Fourier mode with four different amplitudes A with three different radius ratios Γ: (a) $\Gamma = 1.25$, (b) $\Gamma = 1.50$, and (c) $\Gamma = 2$.

good agreement with our conclusions from the energy budget of the linear stability analysis. The instability arises from the mean deceleration and by the interaction of the perturbation with the mean shear through the lift-up or reverse lift-up mechanism. For this case, the Fourier-mode-3 instability can be triggered at a low flow rate because it is the supercritical condition. At higher flow rates, however, the flow is more stable, and a three-periodic inflow perturbation couples only weakly to the relevant shear-induced amplification mechanism. The dominant unstable mode therefore shifts to the first superharmonic of the inflow mode ($m = 6$). This mode extracts kinetic energy from the mean flow more efficiently through the (reverse) lift-up mechanism. These results confirm that the inflow Fourier mode m_{F} strongly influences which linearly unstable Fourier mode is selected by the flow. Yet, all the two-dimensional URANS results with spatially modulated inflow seem to rely on the linear mechanisms identified for the inviscid core-flow model. For the propagation velocity ω_{inst}, we find that it always ranges between 0.15Ω and 0.30Ω.

3. *Effect of radius ratios for* $m_{\mathrm{F}} = 7$

To evaluate the impact of the radius ratio Γ on the instability characteristic, the two-dimensional URANS simulations of the diffuser with three different radius ratios $\Gamma \in \{1.25, 1.50, 2\}$ have been considered. The inlet modulation employs a seven-periodic inflow Fourier mode ($m_{\mathrm{F}} = 7$) with four different amplitudes $A \in \{0, 0.05, 0.15, 0.35\}$. The comparison of propagation velocity ω_{inst} and the mode diagram of the identified instability is depicted in Fig. 9.

For the short diffuser ($\Gamma = 1.25$), the dominant instability Fourier-mode number with mean inflow ($A = 0$) is $m = 8$ [see cyan shadow at the bottom of Fig. 9(a)]. As the seven-periodic Fourier mode ($m_{\mathrm{F}} = 7$) with increasing amplitudes A is applied to the inflow, the Fourier-mode-7 instability ($m = 7$) is triggered [see orange shadow at the bottom of Fig. 9(a)]. Besides, for the highest amplitude $A = 0.35$, higher nonlinear interactions are promoted and superharmonics lead to a Fourier-mode-14 instability [see purple shadow at the bottom of Fig. 9(a)]. The evolution of the instability Fourier-mode number from 8 to 7 and then to 14 with different inlet perturbation amplitudes A under the flow angle $\alpha = 3.32^{\circ}$ is depicted in Fig. 10. We rationalize the two-dimensional (2D) URANS simulations based on the linear stability analysis carried out on the model of Tsujimoto. The inviscid LSA predicts that higher harmonics become linearly unstable at lower inflow angles α_n. In particular, for $\Gamma = 1.25$, the neutral inflow angle predicted by the LSA is $\alpha_n \approx 4.1^{\circ}$ for $m = 14$, while $\alpha_n \approx 5.7^{\circ}$ for $m = 7$ and $\alpha_c^{\mathrm{LSA}} \approx 5.8^{\circ}$ for $m = 8$. Therefore, an inlet forcing with Fourier-inflow mode $m_{\mathrm{F}} = 7$ can select an instability Fourier mode $m = 7$ rather than the linearly critical mode $m_c^{\mathrm{LSA}} = 8$. However, owing to nonlinear interactions in the 2D URANS, a Fourier-inflow mode $m_{\mathrm{F}} = 7$ will produce superharmonics forcing components that can trigger a linear instability at $m = 14$ [see purple region in Fig. 9(a)]. This is expected to occur if the inlet modulation amplitude A is large enough to promote significant nonlinearities as a result of the inlet forcing. It is also expected that for larger inflow Fourier modes, the instability switches from $m = 7$ to $m = 14$ because the strength of the modeled pump impeller wake penetrates

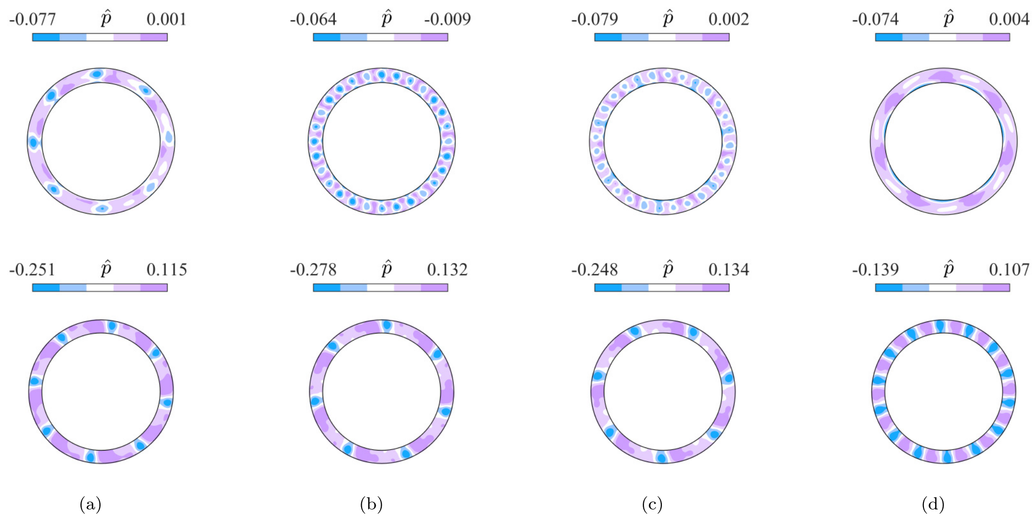

FIG. 10. Phase-averaged static pressure field for the diffuser of radius ratio $\Gamma = 1.25$ under the flow angle 3.40° ($\Phi = 0.34375$) with a seven-periodic inflow Fourier mode $m_\mathrm{F} = 7$ with four different amplitudes A in a reference frame rotate with the inlet radial source flow modulation (top panel) and in a reference frame rotate with the identified instability Fourier mode (bottom panel): (a) $A = 0.00$, (b) $A = 0.05$, (c) $A = 0.15$, and (d) $A = 0.35$.

deeper in the diffuser and allows for perturbation energy production by lift-up and reverse lift-up well in-depth inside the diffuser making advantageous the transfer of energy to higher harmonics ($m = 14$ rather than $m = 7$ for $A > 0.05$). The propagation velocity ω_inst (see Fig. 22 in Appendix D) of the Fourier-mode-14 instability is slower than the other Fourier modes. With the increase of the flow angle α, the propagation velocity ω_inst of Fourier-mode-14 shows a linear downward trend, similar to that reported for a three-dimensional stall in centrifugal pumps (see Ref. [33]). Overall, the instability propagation velocity ω_inst decreases with the increase of the inflow angle α.

Figure 9(c) compares the propagation velocity ω_inst with the mode diagram of the instability identified for the largest diffuser ($\Gamma = 2$) for four different amplitudes of the inflow Fourier modulation $A \in \{0, 0.05, 0.15, 0.35\}$. Concerning the result with mean inflow ($A = 0$), the dominant instability Fourier-mode number is $m = 2$ [see the gray shadow in the bottom of Fig. 9(c)] with the inflow angle $\alpha < 3.92^\circ$ (corresponds to the flow rate ratio $\Phi < 0.375$), which show good consistency with the linear stability analysis diagram [see Fig. 4(c)], while Fourier-mode-3 instability is dominant [see blue shadow at the bottom of Fig. 9(c)] for $\alpha \geqslant 3.92^\circ$ (corresponds to the flow rate ratio $\Phi \geqslant 0.375$). As a seven-periodic Fourier mode is imposed on the inflow, the dominant Fourier-mode-2 instability spreads slightly toward larger flow angles. However, the inflow Fourier mode does not have any major impact on the unstable mode, and only Fourier-mode-2 and 3 perturbations are observed (see Fig. 11). This is due to the amplification mechanism of the instability for $\Gamma = 2$. In fact, such a diffuser ratio is mainly destabilized by the deceleration term I_4'. Hence, controlling the inlet Fourier mode m_F, which would mainly affect the lift-up and reverse lift-up mechanisms, does not have a significant role in this instability as it does not provide any major contribution to I_4'.

4. Comparison with the LSA results

In this section we compare the results of Tsujimoto's model with the more complex flow system represented by the 2D URANS simulations. The aim is to address the absence of several key physical ingredients that may render the application of Tsujimoto's model debatable. In particular, with respect to the realistic configuration of a vaneless diffuser in a centrifugal pump, Tsujimoto's model lacks two- and three-dimensional basic-state features, inflow modulation, kinematic viscosity, and

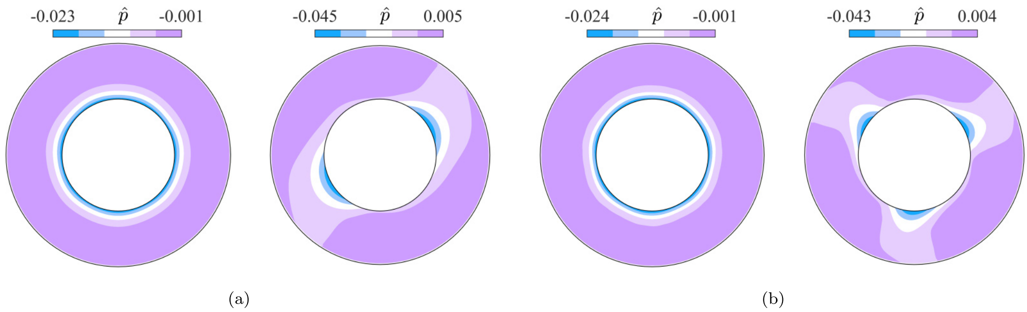

FIG. 11. Phase-averaged static pressure field for the diffuser of radius ratio $\Gamma = 2$ with a seven-periodic inflow Fourier mode $m_{\mathrm{F}} = 7$ with an amplitude $A = 0.05$ in a reference frame rotating with the inlet radial source flow modulation (left panel) and in a reference frame rotating with the identified instability Fourier mode (right panel) under different flow angles: (a) $\alpha = 0$ ($\Phi = 0.25$) and (b) $\alpha = 0$ ($\Phi = 0.5$).

turbulence. Evaluating the agreement between the inviscid LSA and the 2D URANS simulations provides significant insights into the origin of the core-flow instability observed in these two flow representations.

The agreement between Tsujimoto's model and two-dimensional URANS simulations for $A = 0$, i.e., for the URANS simulations without inflow modulation, is remarkable. For $\Gamma = 1.5$, the critical instability Fourier-mode number predicted by the URANS simulations is dominated by $m_c = 5$. This agrees well with the LSA result. Moreover, the critical flow angle ($\alpha_c^{\text{2D-URANS}} \approx 9^\circ$) found by 2D URANS simulations is also very close to the LSA prediction ($\alpha_c^{\text{LSA}} \approx 10^\circ$). The same statement holds true for $\Gamma = 1.25$, where both approaches lead to a critical Fourier mode $m_c^{\text{LSA}} = 8$ occurring at $\alpha_c^{\text{LSA}} \approx 5^\circ$. The LSA result for the widest diffuser we consider, i.e., $\Gamma = 2$, predicts a critical Fourier mode $m_c^{\text{LSA}} = 4$ for $\alpha_c^{\text{LSA}} \approx 16.7^\circ$, while the 2D URANS results point toward an instability occurring at $\alpha_c^{\text{2D-URANS}} \approx 14^\circ$ with a dominant critical Fourier mode $m_c^{\text{2D-URANS}} = 3$. Despite such an apparent discrepancy, the LSA results based on Tsujimoto's model find that the second-most dangerous Fourier mode is $m = 3$, which becomes unstable for inlet angles close to the critical one, i.e., $\alpha_n^{\text{LSA}}(m = 3) = 16.4^\circ$. We stress that such an agreement between the two approaches is remarkable, especially considering that time-marching simulations tend to over-predict the neutral stability limit with respect to a corresponding LSA prediction. A summary of such a good agreement is reported in Table II. Moreover, scaling *ad hoc* the perturbation of the LSA corresponding to the $m_c^{\text{2D-URANS}}$ and adding it to the LSA basic state, Fig. 12 compares the total marginally stable flow obtained using the 2D URANS simulations for $A = 0$ and the model of Tsujimoto. The comparison between the two models is satisfactory, especially considering that, upon a significant intensification of the most dangerous Fourier mode, 2D URANS nonlinearities promote the growth Fourier superharmonics.

Despite the small discrepancies between the uniform ($A = 0$) two-dimensional URANS simulations and the inviscid LSA (attributable to nonlinear interactions and the effects of turbulence and

TABLE II. Comparison of the stability onset predicted by the 2D-URANS simulations for $A = 0$ and the model of Tsujimoto.

Γ	1.25	1.5	2
α_c^{LSA}	5.8°	10.3°	16.7°
$\alpha_c^{\text{2D-URANS}}$	$\in [4.5,\ 5]^\circ$	$\in [9,\ 10]^\circ$	$\in [13.5,\ 14]^\circ$
m_c^{LSA}	8	5	4
$m_c^{\text{2D-URANS}}$	8	5	3

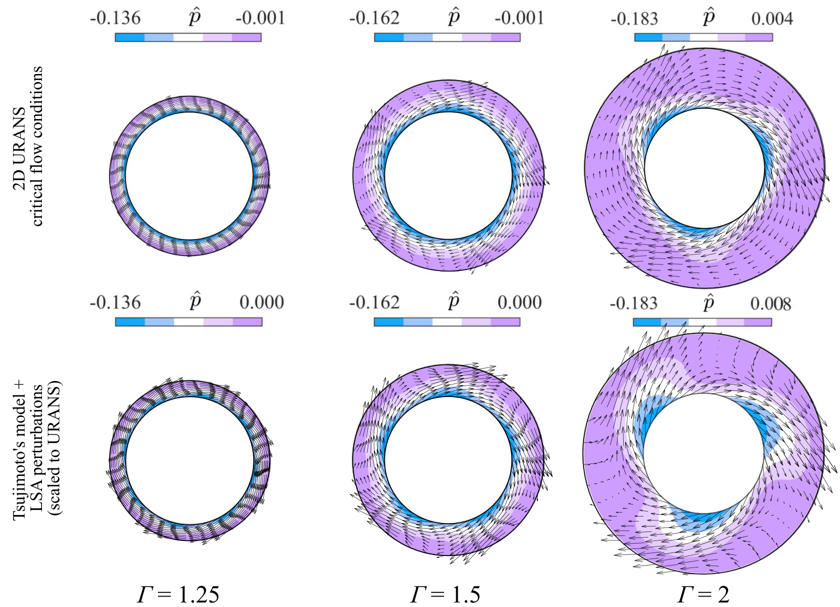

FIG. 12. Snapshot of the flow for the diffusers of radius ratio $\Gamma = 1.25$, 1.5, and 2. Comparison between 2D URANS simulations for $A = 0$ and LSA. The URANS simulations are obtained at slightly supercritical conditions ($\alpha \approx 0.9 \times \alpha_c$). The LSA results for $m_c^{\text{2D-URANS}}$ are obtained by scaling the LSA perturbation such to match the URANS amplitude. Hence, for ease of comparison, the LSA results are plotted at the bottom row with the same scaling of the 2D URANS results.

viscosity) the LSA based on Tsujimoto's model remains effective in identifying the mechanisms responsible for the instability. This supports the conclusion that the observed two-dimensional global instability is fundamentally linear and predominantly inviscid in nature. Moreover, based on the conclusions drawn by the 2D URANS stability diagrams for different m_F, Γ, and A, we infer that the inflow has a limited impact on the origin of the instability; hence, we can speculate that Floquet-like destabilization does not play a significant role in this system when a rotating inflow modulation is considered. This further justifies the use of the LSA energy budget as an interpretation tool to rationalize the URANS destabilization.

C. Three-dimensional effects

For high flow rates, the two-dimensional URANS simulation results still have a significant deviation from the results of previous experimental and numerical simulation studies of the entire centrifugal pump to which this study is inspired. The studies of Ljevar *et al.* [20] suggest that such a high-flow-rate instability is due to a two-dimensional mechanism due to the Fourier nonmodal inflow produced by the pump impeller. However, Appendix A of this study disproves such an interpretation. We are therefore left with an open question on the deviation between 2D URANS results (that do not admit any high-flow-rate instability) and the 3D simulations of the whole centrifugal pump, unstable for two noncontiguous regions at low and high flow rates [33]: Is the high-flow-rate instability due to the presence of the impeller, or can it be reproduced and studied in our idealized system? To provide a proof of principle, three-dimensional numerical simulations for the corresponding vaneless diffuser are carried out. The instability mode diagrams obtained from three-dimensional simulations are summarized and discussed in this section for three different diffuser radius ratios Γ, three values of the azimuthal periodicity m_{F}, and four different amplitudes A of the inflow Fourier modes.

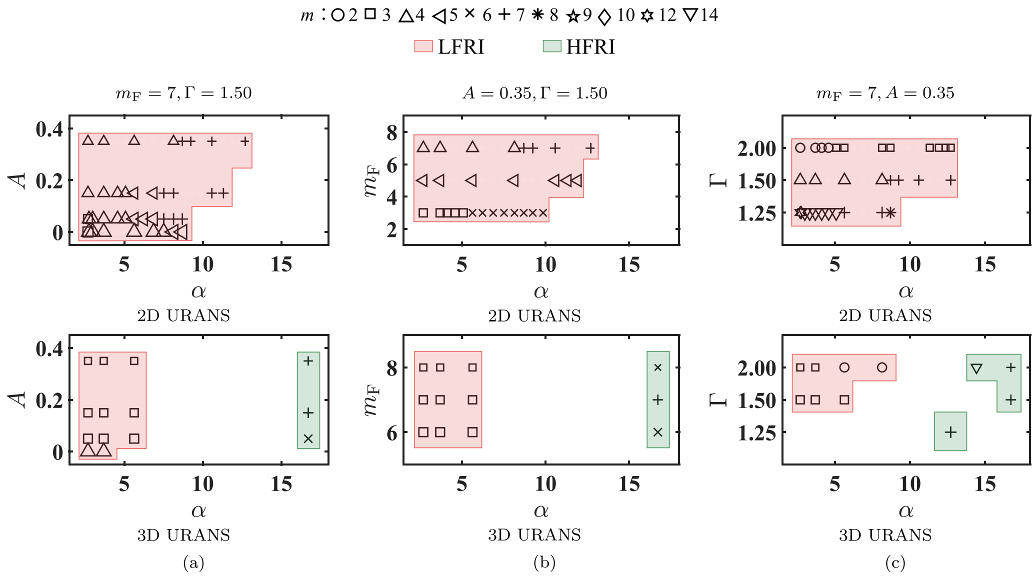

FIG. 13. Comparison of instability characteristic diagram of the flow in the diffuser obtained by two-dimensional (top panel) and three-dimensional (bottom panel) URANS simulations: (a) constant inflow Fourier-mode number m_F and radius ratio Γ with variable inflow perturbation amplitude A, (b) constant inflow perturbation amplitude A and radius ratio Γ with variable inflow Fourier-mode number m_F, and (c) constant inflow Fourier-mode number m_F and perturbation amplitude A with variable radius ratio Γ.

Figure 13(a) depicts the comparison of the Fourier-mode diagram of the instability identified for the diffuser with $\Gamma = 1.50$ (consistent with the experimental setup [30–34]) whose mean inlet profile is fitted from a numerical zero-leakage configuration with four different amplitudes of the Fourier mode $A \in \{0, 0.05, 0.15, 0.35\}$. The three-dimensional flow field shows significant differences compared with the results of the two-dimensional simulations. Focusing on the result for the homogeneous inflow ($A = 0$), the Fourier-mode-4 instability is dominant in the 3D URANS simulations, which is consistent with the two-dimensional radial source flow at the same inflow angles. However, in three dimensions, such instability only occurs with the flow angle $\alpha < 5.63^\circ$ (corresponding to the flow rate ratio $\Phi = 0.375$), while the unstable range predicted by our 2D URANS simulations is twice as extended. As the flow angle α increases, the three-dimensional flow field becomes chaotic. No other instabilities are apparent in our 3D URANS for $A = 0$ above $\alpha = 5.63^\circ$. We speculate that this stabilization is due to the presence of boundary layers at the diffuser walls because they tend to decelerate the flow at the hub and the shroud, accelerating it at the diffuser core. De facto, this leads to a reduction of the local flow angle for the core-flow, leading to a stabilization of the two-dimensional inviscid mechanism responsible for destabilizing the model of Tsujimoto and our 2D URANS flow.

On top of the three-dimensional simulations for the homogeneous inflow, we compared the flow field under a seven-periodic inflow perturbation with the amplitude $A = 0.05$ at the critical flow angle of the low-flow rate instability ($\alpha = \alpha_c$) obtained by linear stability analysis model, two-dimensional URANS, and three-dimensional URANS simulations. Figure 14(a) shows that the mean separation of the three-dimensional flow has a significant impact on the flow at $\alpha \approx 9^\circ$. Based on the top-right panel of Fig. 14(a), the two-dimensional analysis does not apply to any region of the three-dimensional vaneless diffuser flow. Hence, for $\alpha \approx 9^\circ$, the discrepancy between 2D and 3D URANS is not surprising. As a seven-periodic Fourier mode is imposed on the inflow ($A > 0$), the previously dominant Fourier-mode-4 instability observed for $\alpha \approx 5^\circ$ in 3D flows with $\Gamma = 1.5$ is taken over by the critical Fourier-mode 3. The consistent results of our simulations seem to suggest that the 3D flow is always more stable than the corresponding 2D flow at low flow angles. However,

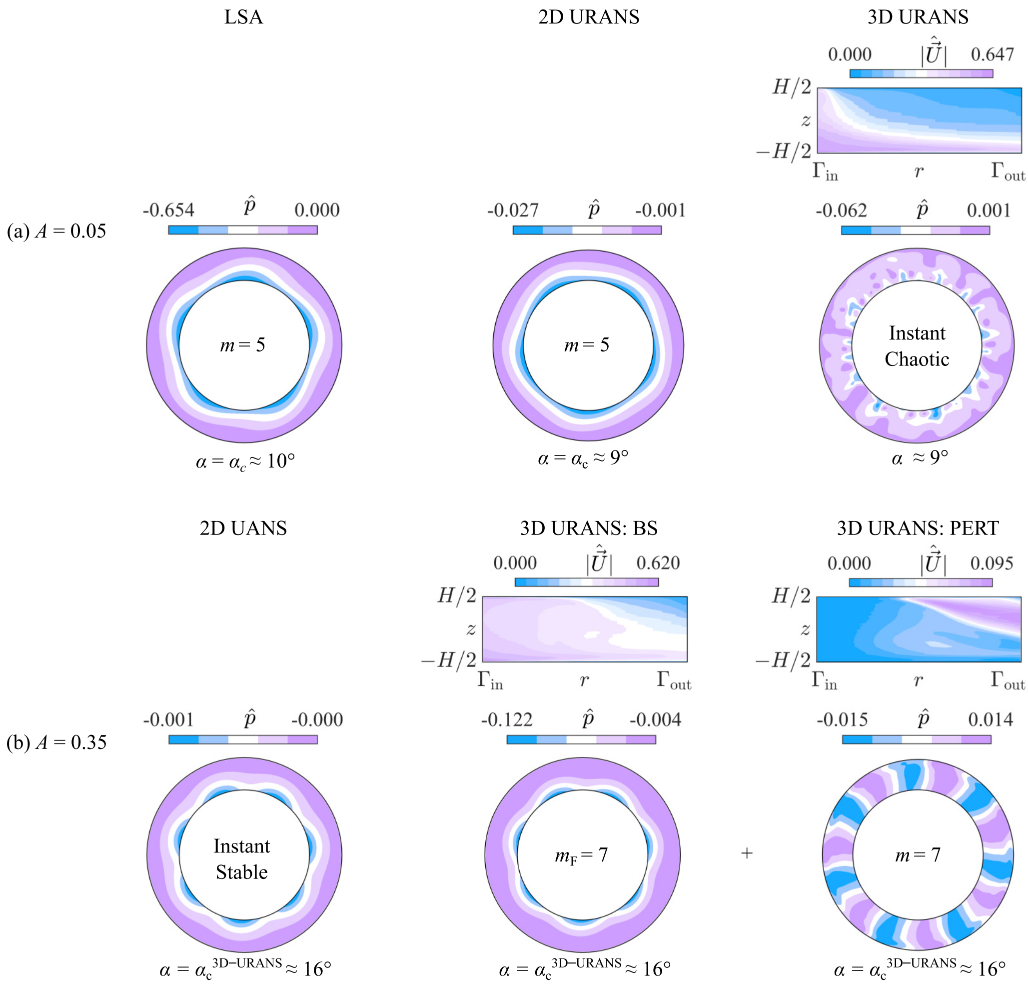

FIG. 14. Comparison of phase-averaged flow fields at the critical flow angle for the low-flow-rate instability ($\alpha = \alpha_c$) under a seven-periodic inflow perturbation with two different amplitudes: (a) $A = 0.05$ and (b) $A = 0.35$, obtained using different approaches (linear stability analysis, two-dimensional URANS, and three-dimensional URANS simulations).

a more robust comparative analysis with a large eddy simulation (LES) would be needed to be conclusive on the artifacts potentially due to the turbulence model.

Another major difference between our 2D URANS and 3D URANS is observed at high flow rates, where a 3D instability is reported for a flow angle $\alpha \approx 16.72^\circ$ (corresponding to the flow rate ratio $\Phi = 1.125$). This occurs in the presence of a non-negligible inflow modulation ($A > 0$). For the lowest inflow Fourier amplitude $A = 0.05$, the perturbation is the weakest and Fourier-mode-6 instability is triggered. For the other two higher inflow Fourier amplitudes ($A \in \{0.15, 0.35\}$), the instability wave number at the large flow angle is influenced by the inflow Fourier modes [see Fig. 13(b)], with propagation velocity $\omega_{\rm inst}/\Omega \in [0.121, 0.125]$ which is lower than the low-flow angle instability (not shown). The same Fourier-mode-7 instability is also observed in our previous study on a three-dimensional whole pump model [33], hence we intend the present 3D URANS for our idealized system as a proof of principle that high-flow-rate instabilities can be studied in the vaneless diffuser without the need to simulate the whole centrifugal pump.

To better characterize the mechanism of high-flow-rate instability, we compared the flow field under a seven-periodic inflow perturbation with the amplitude $A = 0.35$ at $\alpha = \alpha_c \approx 16^\circ$ obtained by two-dimensional and three-dimensional URANS simulations as depicted in Fig. 14(b). The evidence resulting from our simulations points to a mechanism connected with the three-dimensional configuration. The middle panel of Fig. 14(b) shows that the perturbation velocity becomes very strong in correspondence with the phase-averaged separation of the boundary layer at $z = H/2R_1$, which is an indication that the flow separation is either responsible for or results from the instability. However, the presence of such a pronounced separation of the boundary layer tends to limit the analysis we can reliably perform by using URANS. A detailed investigation is currently planned in a future study making use of LESs rather than URANS and carrying out a stability analysis whose energy budget could be insightful into the origin of the observed high-flow-rate instability.

Figure 13(b) depicts the comparison of instability characteristics identified for the diffuser with $\Gamma = 1.50$ with a mean inlet profile fitted from a numerical zero-leakage configuration with three different periodicities of inflow Fourier modes $m_F \in \{6, 7, 8\}$ with the amplitude $A = 0.35$. The results show that the inflow Fourier-mode number m_F does not change the low flow rate instability Fourier-mode number but significantly changes the Fourier-mode number of the large flow rate instability. Concerning the propagation velocity, it always remains $\omega_{\text{inst}}/\Omega = 0.125$.

Figure 13(c) depicts the comparison of instability characteristics identified for the diffuser with three different radius ratios $\Gamma \in \{1.25, 1.50, 2.00\}$ with a mean inlet profile fitted from the zero-leakage numerical configuration with an amplitude $A = 0.35$. The results show that, for the shortest diffuser $\Gamma = 1.25$, the flow field is chaotic at low flow angles, and only the large-flow-rate instability is observed in our 3D URANS. For the largest diffuser $\Gamma = 2$, the low-flow-rate instability is here reported up to a larger inflow angle. The low-flow-rate instability Fourier-mode number is also different under different flow angles, passing from a Fourier-mode 3 to a Fourier-mode 2. Such a change of mode with the inflow angle is also observed to occur for the high-flow-rate instability reported in our largest diffuser.

V. CONCLUSIONS

A comprehensive investigation of the instabilities in a radial source flow between parallel annular plates under spatially-modulated-inlet boundary conditions with an angular rotational speed of Ω is conducted in this study, using a combination of theoretical modeling and two- and three-dimensional URANS simulations. Different levels of complexity have gradually evolved in the radial source flow model to explain the different instabilities identified in the experiments carried out in our previous studies and to trace back the physical mechanisms responsible for the instabilities.

By conducting a linear stability analysis employing the one-dimensional model of Tsujimoto *et al.* [19] with the assumption that the flow is inviscid and homogeneous in the θ direction, we demonstrate that the traditional core-flow instability can be predicted by this model. Moreover, performing an energy-budget analysis on the critical perturbation indicated that the low-flow-rate instability originates from the contributions of lift-up and flow deceleration mechanisms. However, the linear approach is unable to distinguish the dominant Fourier mode for $\alpha \ll \alpha_c$ because the nonlinear interactions between different Fourier modes are not accounted for.

To understand the effect of inflow modulation in θ on the instability and the nonlinearities for strongly supercritical conditions, two-dimensional URANS simulations that consider a periodic perturbation imposed on the inflow have been performed. The results show good consistency with the two-dimensional linear approach at $\alpha \approx \alpha_c$. The instabilities are all consistent with the two-dimensional mean flow linear instability. At the same time, the linearly unstable Fourier mode is affected by the inflow Fourier mode used to model the impeller wake. However, these instabilities still arise from the same mechanisms identified by the two-dimensional linear stability analysis. Our results therefore demonstrate that the global core-flow instability is of an inviscid and linear nature. Moreover, the comparison between LSA and 2D URANS suggests that the swirling inflow modulation does not trigger Floquet-type destabilizations. On top, in view of the agreement between

Tsujimoto's model and 2D URANS simulations, our results suggest that Coriolis and centrifugal instabilities are unlikely to be the primary mechanisms responsible for the core-flow instability observed in the vaneless diffuser at low flow rates.

For low aspect ratios $\Gamma \in \{1.25, 1.5\}$, the perturbation growth relates to lift-up and reverse lift-up mechanisms, and therefore the inlet Fourier mode m_{F} provides a significant parameter of control of the instability. Indeed, m_{F} provides additional shear layers, hence it promotes I_2' and I_3', which are the main destabilizing terms for $\Gamma = 1.25$ and 1.50. On the other hand, the linear instability mechanism for large diffusers relies on flow deceleration as the main contribution to the perturbation energy growth. This makes the instability almost insensitive to m_{F} for $\Gamma = 2$.

Given that the LSA carried out on Tsujimoto's model identifies either shear-driven or deceleration-driven instabilities, the interpretation provided by the corresponding energy budget is expected to have significance in the understanding of low-flow-rate instabilities in vaneless diffusers installed on turbomachines. In particular, as low-radius ratios ($\Gamma = 1.25$ and 1.5) are destabilized primarily by shear, the inflow modulation, hence the number of impeller blades before the vaneless diffuser, is expected to have an impact on the stall of the whole machine. On the other hand, if a vaneless diffuser with high radius ratio is installed, the main destabilization source is due to the radial deceleration of the flow; hence the number of impeller blades is not expected to impact the pump low-flow-rate stall of the pump connected to the vaneless diffuser. This is supported by our 2D-URANS simulations, which make such conclusions robust against nonlinearities and strong deviations from the critical condition.

A long-lasting debate in the turbomachine community deals with the origin of the low-flow-rate instabilities observed in vaneless diffusers. In particular, the open question is whether such instabilities can be traced back to boundary-layer instabilities at the hub or shroud or if the vaneless diffusers are rather limited by the core-flow instability at low flow rates. To study the boundary layer effect on the instabilities, a three-dimensional model with a multistage scale-like-matching fitted inflow profile has been simulated and compared with the corresponding two-dimensional simulations. Two different instability mechanisms are found in the three-dimensional system: (i) at low flow rates, we found that the two-dimensional core-flow instability is controlled by the inflow angle, and (ii) at high flow rates, we found that three-dimensional flow leads to an instability that has not been observed in the 2D system. The low-flow-rate mechanism observed at low flow angles can be understood solely by considering the skewness of the diffuser inflow in a one-dimensional inviscid linear stability analysis, without incorporating any inhomogeneous forcing in the θ direction. Our simulations suggest that a three-dimensional flow stabilizes the low-flow-rate core flow and delays the onset of such instability. We speculate that such a stabilization is due to the presence of the boundary layers on the diffuser walls. In fact, given Φ, a deceleration at the walls leads to an acceleration of the core flow, hence to an increase of the inflow angle. The second instability regime that occurs at large flow angles is associated with even weak inflow modulations. Further investigations are planned for a better understanding of this three-dimensional instability; however, we stress that such a destabilization has been previously observed in one of our studies in which we simulate the whole centrifugal pump [32,34].

From a practical point of view, the insights reported in this paper can provide avenues for improving the design of radial diffusers with the aim of increasing their stable operating range, particularly concerning the instability that appears at lower flow rates, which is also the most frequently reported in real applications. It has been shown that two mechanisms are responsible for the development of this instability:

(1) The lift-up and reverse lift-up mechanisms are governed by the shear distribution in the basic flow. Because the impeller blade count affects this distribution, varying the number of blades may alter the strength of these mechanisms and thereby modify the stable operating range of the machine. However, blade count also influences pump performance, so any stability improvement is likely to involve a trade-off with efficiency, pressure rise, or other performance metrics.

(2) The second identified mechanism is related to the deceleration of the flow. This is limiting for design because this mechanism is linked to the very function of the diffuser. Nevertheless,

our simulations suggest that three-dimensional flow features are stabilizing with respect to this mechanism by increasing the mean inflow angle of the core flow. This finding could pave the way for control methods that further influence the structure of this flow to extend the range of operability of the diffuser.

ACKNOWLEDGMENTS

This research was supported by the Grand Équipement National De Calcul Intensif (GENCI) for providing the computational resources under Project No. A0102A01741. Additional funding was provided by CSC (China Scholarship Council) in support of the doctoral studies of M.F. (CSC ID: 201908320328).

DATA AVAILABILITY

The data that support the findings of this article are not publicly available upon publication because it is not technically feasible and/or the cost of preparing, depositing, and hosting the data would be prohibitive within the terms of this research project. The data are available from the authors upon reasonable request.

APPENDIX A: DIFFERENCE BETWEEN THIS STUDY AND THE SIMULATIONS BY LJEVAR *ET AL.*

In our previous study of a vaneless diffuser installed on a centrifugal machine [33,34], we identified two distinct instabilities. The first is the low-flow-rate mean core flow instability, which was accurately predicted by both our one-dimensional linear stability analysis and two-dimensional URANS simulation. The second one occurs at large flow rates, and we speculated that it could be due to the inlet-modulated radial swirling source flow. Ljevar *et al.* [20] reported a similar phenomenon for two-dimensional flows with Fourier nonmodal inlet wakes; however, their analysis is rather qualitative and does not pinpoint the role of the modulated radial swirling source in the instability mechanism. In our previous sections, we successfully manage to reproduce the flow instability for high values of Φ, but we demonstrate that such instability is not due to the inlet-modulated radial swirling source but is only controlled by it.

There are, however, two key differences between our two-dimensional URANS simulation and that of Ref. [20]. First, in our simulation, the inlet perturbation affects both U_r and U_θ, whereas in Ljevar *et al.*'s simulation, the inlet perturbation only affects U_r. Second, we used a single Fourier mode to mimic the inflow pump impeller wake, while Ljevar *et al.* used a Fourier-nonmodal function for this purpose.

1. Comparison between averaged and modulated tangential velocity for $m_F = 7$

To investigate the role of inlet modulation and better compare with the works of Ljevar *et al.* [20] on 2D simulation of vaneless diffusers, we also tested the inlet boundary condition whose Fourier mode only perturbs the radial velocity U_r. The difference between the two inlet boundary conditions is depicted in Fig. 15. The comparison of the instability diagram of the diffuser under two different inflow boundary conditions is summarized in Fig. 16. In this analysis, we set a constant radius ratio $\Gamma = 1.50$ and a seven-periodic inflow Fourier mode ($m_\mathrm{F} = 7$) with four different amplitudes $A \in \{0.00, 0.05, 0.15, 0.35\}$.

Concerning the simulation result of the diffuser with the inflow Fourier mode only perturbs U_r, the instability Fourier-mode diagram [bottom panel of Fig. 16(b)] does not change much compared with the simulation result with the inflow Fourier mode perturbs both U_r and U_θ [bottom panel of Fig. 16(a)]. The most significant difference is that the onset of flow instability occurs at higher inflow angles with the second inflow boundary condition. For the instability propagation velocity ω_{inst} [top panels of Figs. 16(a) and 16(b)], neither the trend nor the magnitude produced much change under the two different inflow boundary conditions.

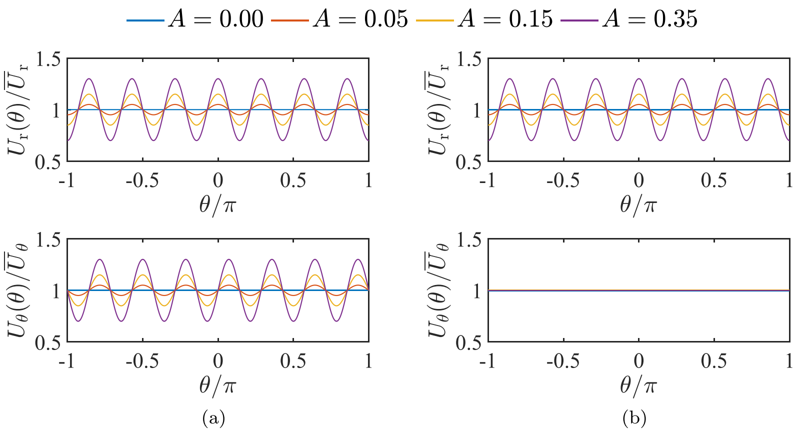

FIG. 15. The inlet-modulated radial swirling source inflow boundary conditions are mimicked by a seven-periodic Fourier mode with four different amplitudes A: (a) the Fourier mode perturbs both U_r (cos function) and U_θ (sin function) and (b) the Fourier mode only perturbs U_r.

Here we can conclude that these two inflow boundary conditions do not lead to much change in the simulation results; the biggest difference between the two is that the second boundary condition leads to a larger critical flow angle α_c, probably due to the flow gradients induced in the bulk by the continuity equation. This is one of the reasons why, in Ljevars' study, they observed the periodic instability Fourier mode near the design flow rate Φ_d. We, however, stress that the inlet condition used in our study with a Fourier mode perturbs both U_r and U_θ and is closer to the physical perturbations that we observed in our previous experiment.

For the first difference in the boundary conditions, we show that this difference does not significantly affect the results of our two-dimensional URANS simulations, and the identified instabilities always depend on the linear instability of the mean core flow, rather than on the instability of the

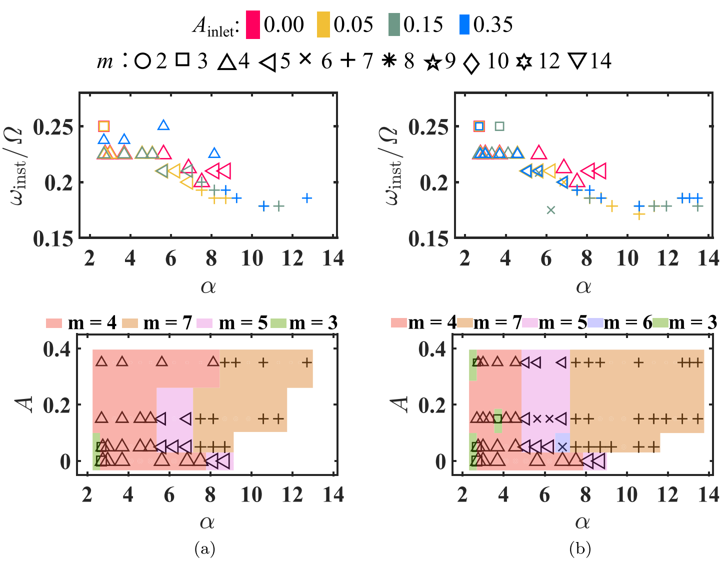

FIG. 16. Instability characteristic diagram of the flow in the diffuser of radius ratio $\Gamma = 1.50$ with a seven-periodic inflow Fourier mode with four different amplitudes A: (a) the Fourier mode perturbs both U_r (cos function) and U_θ (sin function) and (b) the Fourier mode only perturbs U_r.

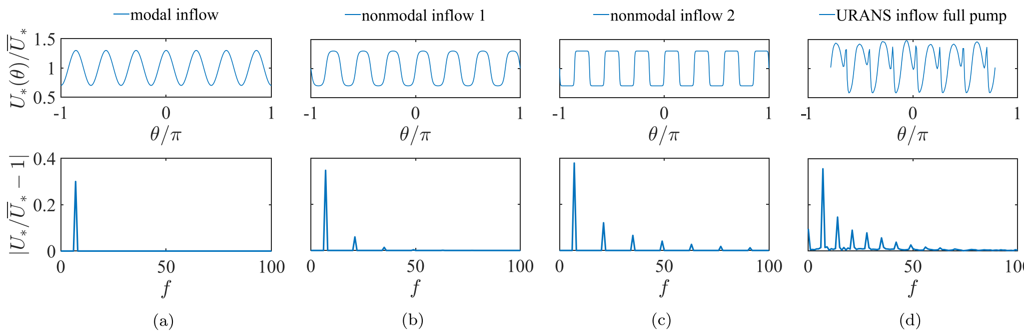

FIG. 17. The comparison of inlet-modulated radial swirling source inflow boundary condition with seven-periodic mimicked by different functions and obtained by URANS simulation: (a) Fourier-modal inflow perturbation, i.e., a single Fourier mode, (b) Fourier-nonmodal inflow perturbation with a smaller steepness, (c) Fourier-nonmodal inflow perturbation with a larger steepness, and (d) numerical inflow perturbation obtained by 3D URANS of the full pump evaluated at the vaneless diffuser inlet midheight.

inlet-modulated radial swirling source flow. The only significant difference is that the flow instability occurs at slightly higher inflow angles with the inlet perturbation only disturbing U_r.

2. Comparison between Fourier-modal and Fourier-nonmodal inflow modulation $m_F = 7$

To investigate the importance of the second difference between our inflow and that of Ljevar *et al.*, we test our simulation cases with Fourier-nonmodal inflow perturbations described by the periodic hyperbolic tangent function:

$$U_r(\theta) = \overline{U}_r\left[1 + A\frac{\tanh(DY_r(\theta))}{\tanh(D)}\right], \tag{A1a}$$

$$U_\theta(\theta) = \overline{U}_\theta\left[1 + A\frac{\tanh(DY_\theta(\theta))}{\tanh(D)}\right], \tag{A1b}$$

where the D indicates the steepness of the inlet modulation function, and $Y_{r,\theta}(\theta)$ yields

$$Y_r(\theta) = \cos[m_\mathrm{F}(\theta - \Omega t)], \tag{A2a}$$

$$Y_\theta(\theta) = \sin[m_\mathrm{F}(\theta - \Omega t)], \tag{A2b}$$

where t is the time and m_F is the number of mimicked pump impeller wake around the circumference. The inlet-modulated radial swirling source inflow boundary conditions mimicked by Fourier-modal and Fourier-nonmodal functions are demonstrated in Fig. 17.

The comparison of propagation velocity ω_inst and Fourier-mode diagram of the instability identified for the radius ratio $\Gamma = 1.50$ with a seven-periodic inflow perturbation with four different amplitudes $A \in \{0, 0.05, 0.15, 0.35\}$ mimicked by Fourier-modal and Fourier-nonmodal functions imposed to the inflow are depicted in Fig. 18. By comparing the simulation results with Fourier-nonmodal inflow perturbation and a low steepness of $D = 2$ [see Fig. 18(b)] to the results with Fourier-modal inflow perturbation [see Fig. 18(a)], we can find that the Fourier-nonmodal inflow perturbation leads to more complex nonlinear interactions and slightly changes the stability diagram. Regarding the simulation results with Fourier-nonmodal inflow perturbation with a large steepness [see $D = 1000$ in Fig. 18(c)], the instability Fourier-mode diagram becomes more complex due to stronger nonlinearities. Besides, we can find that the instability occurs at slightly higher inflow angles under the Fourier-nonmodal inlet perturbation; however, the overall comparison between the critical conditions for these three very different inflow modulations is minimal. Hence, the instability remains a linear instability of the mean core flow rather than an inlet-modulated radial swirling

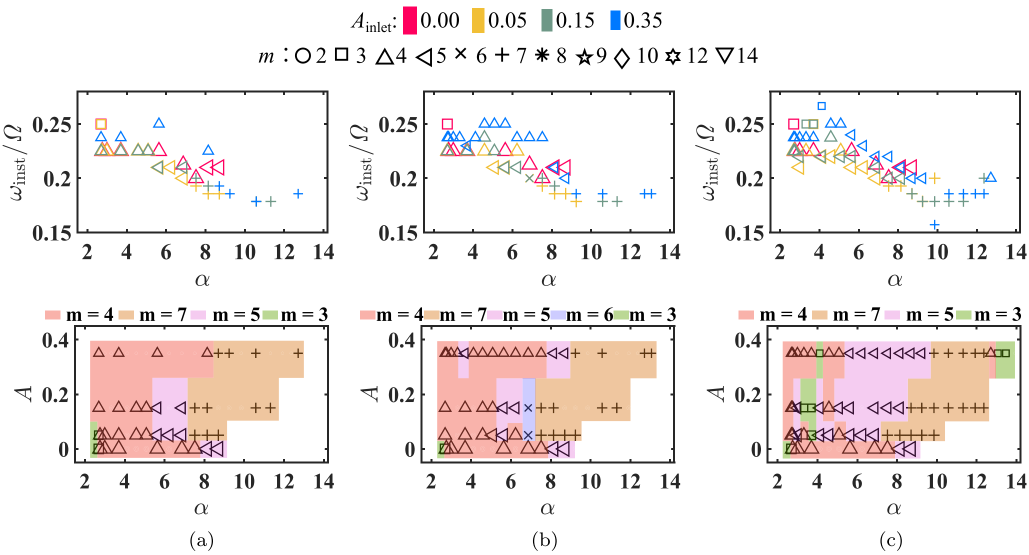

FIG. 18. Instability characteristic diagram of the flow in the diffuser of radius ratio $\Gamma = 1.50$ with a seven-periodic inflow perturbation with four different amplitudes A Fourier-modal and Fourier-nonmodal inflow perturbation mimicked by three different functions: (a) Fourier-modal inflow perturbation, i.e., a single Fourier mode, (b) Fourier-nonmodal inflow perturbation with a smoother slope, and (c) Fourier-nonmodal inflow perturbation with a sharper slope.

source instability as speculated by Ljevar *et al.* [20]. The enhanced α_c due to an inlet modulation is rather to be intended as an easier destabilization of a Fourier-nonmodal perturbed flow.

APPENDIX B: SOLUTIONS OF LINEAR STABILITY ANALYSIS

In cylindrical coordinates, the two-dimensional continuity equation for an incompressible flow takes the form

$$\frac{\partial \overline{\rho}}{\partial \overline{t}} = 0 \text{ and } \frac{\partial \overline{U}_z}{\partial \overline{t}} = 0. \tag{B1}$$

For an inviscid flow, the two-dimensional momentum equation in cylindrical coordinates yields

$$\frac{\partial U_r}{\partial t} + U_r \frac{\partial U_r}{\partial r} + \frac{U_\theta}{r}\frac{\partial U_r}{\partial \theta} - \frac{U_\theta^2}{r} = -\frac{\partial P}{\partial r}, \tag{B2}$$

$$\frac{\partial U_\theta}{\partial t} + U_r \frac{\partial U_\theta}{\partial r} + \frac{U_\theta}{r}\frac{\partial U_\theta}{\partial \theta} + \frac{U_r U_\theta}{r} = -\frac{1}{r}\frac{\partial P}{\partial \theta}. \tag{B3}$$

Taking the curl of the Euler equation leads to the vorticity equation:

$$\frac{\partial \zeta}{\partial t} + U_r \frac{\partial \zeta}{\partial r} + \frac{U_\theta}{r}\frac{\partial \zeta}{\partial \theta} = 0, \tag{B4}$$

where $\nabla \times \boldsymbol{U} = \zeta \boldsymbol{U}_z$ and $\zeta = r^{-1}\partial_r(rU_\theta) - r^{-1}\partial_\theta U_r$ denotes the vorticity.

Substituting the LSA flow ansatz [see (15)] and the basic state solution of Tsujimoto's model, we arrive at the linearized governing equations for the perturbation:

$$\frac{\partial (r u_r')}{\partial r} + \frac{\partial u_\theta'}{\partial \theta} = 0, \tag{B5}$$

$$\frac{\partial u_r'}{\partial t} - \frac{u_r'}{r^2} + \frac{1}{r}\frac{\partial u_r'}{\partial r} + \frac{\mu}{r^2}\frac{\partial u_r'}{\partial \theta} - \frac{2\mu}{r^2}u_\theta' = -\frac{\partial p'}{\partial r}, \tag{B6}$$

$$\frac{\partial u'_\theta}{\partial t} + \frac{1}{r}\frac{\partial u'_\theta}{\partial r} + \frac{u'_\theta}{r^2} + \frac{\mu}{r^2}\frac{\partial u'_\theta}{\partial \theta} = -\frac{1}{r}\frac{\partial p'}{\partial \theta}, \tag{B7}$$

$$\frac{\partial \zeta'}{\partial t} + \frac{1}{r}\frac{\partial \zeta'}{\partial r} + \frac{\mu}{r^2}\frac{\partial \zeta'}{\partial \theta} = 0, \tag{B8}$$

$$\frac{1}{r}\frac{\partial (r u'_\theta)}{\partial r} - \frac{1}{r}\frac{\partial u'_r}{\partial \theta} = \zeta', \tag{B9}$$

where ζ' denotes the infinitesimal vorticity perturbation.

Substituting the normal-mode expressions into (B5)–(B9) yields

$$\frac{\partial (r\tilde{u}_r)}{\partial r} - im\tilde{u}_\theta = 0, \tag{B10}$$

$$i\xi\tilde{u}_r - \frac{\tilde{u}_r}{r^2} + \frac{1}{r}\frac{\partial \tilde{u}_r}{\partial r} - \frac{im\mu}{r^2}\tilde{u}_r - \frac{2\mu}{r^2}\tilde{u}_\theta = -\frac{\partial \tilde{p}}{\partial r}, \tag{B11}$$

$$i\xi\tilde{u}_\theta + \frac{1}{r}\frac{\partial \tilde{u}_\theta}{\partial r} + \frac{\tilde{u}_\theta}{r^2} - im\frac{\mu}{r^2}\tilde{u}_\theta = \frac{1}{r}im\tilde{p}, \tag{B12}$$

$$i\xi\tilde{\zeta} + \frac{1}{r}\frac{\partial \tilde{\zeta}}{\partial r} - im\frac{\mu}{r^2}\tilde{\zeta} = 0, \tag{B13}$$

$$\frac{1}{r}\frac{\partial (r\tilde{u}_\theta)}{\partial r} + \frac{im}{r}\tilde{u}_r = \tilde{\zeta}. \tag{B14}$$

The neutral stability condition is obtained by setting the growth rate σ to zero, which characterizes the onset of rotating instability at the critical state.

The general solution of (B13) is given by

$$\tilde{\zeta}(r) = C\exp\left[\frac{i\chi}{2}(1-r^2) + im\mu\ln(r)\right], \tag{B15}$$

where $C = \tilde{\zeta}(r=1)$. Substituting this solution into (B14), one obtains

$$C\exp\left[\frac{i\chi}{2}(1-r^2) + im\mu\ln(r)\right] = \frac{1}{r}\frac{\partial (r\tilde{u}_\theta)}{\partial r} + \frac{im}{r}\tilde{u}_r, \tag{B16}$$

together with (B10), the velocity perturbations are expanded in separated variables:

$$\tilde{u}_r = a_1 F + a_2 G, \quad \tilde{u}_\theta = b_1 F + b_2 G, \tag{B17}$$

where F and G are two arbitrary functions of r, and a_1, a_2, b_1, and b_2 are constants to be determined. Substitution of (B17) into (B10) and (B16) leads to

$$\begin{aligned} &a_1\frac{\partial (rF)}{\partial r} + a_2\frac{\partial (rG)}{\partial r} - im(b_1F + b_2G) = 0,\\ &b_1\frac{\partial (rF)}{\partial r} + b_2\frac{\partial (rG)}{\partial r} + im(a_1F + a_2G) = C\exp\left[\frac{i\chi}{2}(1-r^2) + im\mu\ln(r)\right], \end{aligned} \tag{B18}$$

the first equation in (B18) can be rearranged as

$$\frac{\partial (rF)}{\partial r} = -\frac{a_2}{a_1}\frac{\partial (rG)}{\partial r} + im\frac{b_1}{a_1}F + im\frac{b_2}{a_1}G, \tag{B19}$$

by substituting (B19) into the second equation of (B18), the following expression is obtained:

$$\frac{\partial (rG)}{\partial r}\left(b_2 - \frac{b_1a_2}{a_1}\right) + imG\left(a_2 + \frac{b_1b_2}{a_1}\right) + imF\left(a_1 + \frac{b_1^2}{a_1}\right) = C\exp\left[\frac{i\chi}{2}(1-r^2) + im\mu\ln(r)\right]. \tag{B20}$$

Similarly, one can also derive

$$\frac{\partial(rG)}{\partial r} = -\frac{a_1}{a_2}\frac{\partial(rF)}{\partial r} + im\frac{b_1}{a_2}F + im\frac{b_2}{a_2}G, \tag{B21}$$

$$\frac{\partial(rF)}{\partial r}\left(b_1 - \frac{b_2 a_1}{a_2}\right) + imF\left(a_1 + \frac{b_1 b_2}{a_2}\right) + imF\left(a_1 + \frac{b_2^2}{a_2}\right) = C\exp\left[\frac{i\chi}{2}(1-r^2) + im\mu\ln(r)\right]. \tag{B22}$$

The orthogonality conditions associated with (B19) and (B21) yield

$$\begin{aligned} a_1 &= -i, \quad b_1 = 1,\\ a_2 &= -i, \quad b_2 = -1. \end{aligned} \tag{B23}$$

consequently, (B20) and (B22) reduce to

$$\begin{aligned} -2\frac{\partial(rG)}{\partial r} + 2mG &= rC\exp\left[\frac{i\chi}{2}(1-r^2) + im\mu\ln(r)\right],\\ 2\frac{\partial(rF)}{\partial r} + 2mF &= rC\exp\left[\frac{i\chi}{2}(1-r^2) + im\mu\ln(r)\right]. \end{aligned} \tag{B24}$$

The general solutions of F and G consist of a particular solution of the nonhomogeneous equations and a solution of the corresponding homogeneous equations and can be written as

$$\begin{aligned} F(r) &= F_p(r) + F_h(r),\\ G(r) &= G_p(r) + G_h(r), \end{aligned} \tag{B25}$$

where the subscript p denotes the particular solution and h denotes the solution of the corresponding homogeneous equation. For the particular solution, we propose the following form:

$$\begin{aligned} F_p(r) &= \frac{1}{2}\int_1^r e^{\frac{-i\xi}{2}(r_0^2-1)+im\mu\ln r_0}\left(\frac{r_0}{r}\right)^{n+1} dr_0,\\ G_p(r) &= \frac{1}{2}\int_r^\Gamma e^{\frac{-i\xi}{2}(r_0^2-1)+in\mu\ln r_0}\left(\frac{r}{r_0}\right)^{n-1} dr_0. \end{aligned} \tag{B26}$$

The corresponding homogeneous equations for another solution are

$$\begin{aligned} -\frac{\partial(rG_h)}{\partial r} + mG_h &= 0,\\ \frac{\partial(rF_h)}{\partial r} + mF_h &= 0, \end{aligned} \tag{B27}$$

from which the solutions are readily obtained as

$$\begin{aligned} F_h(r) &= \frac{C_1}{r^{m+1}},\\ G_h(r) &= C_2 r^{m-1}, \end{aligned} \tag{B28}$$

accordingly, the solutions of F and G are expressed as

$$\begin{aligned} F(r) &= F_p(r) + \frac{C_1}{r^{m+1}},\\ G(r) &= G_p(r) + C_2 r^{m-1}. \end{aligned} \tag{B29}$$

Substituting these solutions into (B17), the velocity perturbations are obtained as

$$\begin{aligned} \tilde{u}_r &= -i\left[C(F_\eta + G_\eta) + \tfrac{C_1}{r^{m+1}} + C_2 r^{m-1}\right],\\ \tilde{u}_\theta &= C(F_\eta - G_\eta) + \tfrac{C_1}{r^{m+1}} - C_2 r^{m-1}, \end{aligned} \tag{B30}$$

with

$$F_\eta(r) = \frac{1}{2}\int_1^r e^{-\frac{i\xi}{2}(r_0^2-1)+im\mu\ln r_0}\left(\frac{r_0}{r}\right)^{m+1} dr_0,$$
$$G_\eta(r) = \frac{1}{2}\int_r^\Gamma e^{-\frac{i\xi}{2}(r_0^2-1)+im\mu\ln r_0}\left(\frac{r}{r_0}\right)^{m-1} dr_0. \tag{B31}$$

The constants C_1 and C_2 are determined from the inlet boundary conditions at the diffuser inlet $r = 1$:

$$\tilde{u}_r(r=1) = \tilde{u}_\theta(r=1) = 0, \tag{B32}$$

which yields

$$\tilde{u}_r(r=1) = -i\{C[F_\eta(r=1) + G_\eta(r=1)] + C_1 + C_2\} = 0,$$
$$\tilde{u}_\theta(r=1) = C[F_\eta(r=1) - G_\eta(r=1)] + C_1 - C_2 = 0, \tag{B33}$$

since $F_\eta(r=1) = 0$, (B31) gives

$$C_1 = 0,$$
$$C_2 = -CG_\eta(r=1), \tag{B34}$$

As a result, the velocity perturbations can be finally written as

$$\tilde{u}_r = -iC[F_\eta + G_\eta - G_\eta(r=1)r^{m-1}],$$
$$u_\theta = C[F - G + G(r=1)r^{m-1}], \tag{B35}$$

at the diffuser outlet, which is directly connected to the atmosphere, the pressure perturbation satisfies $\tilde{p}(r=\Gamma) = 0$. Therefore, (B12) reduces to

$$i\xi\tilde{u}_\theta(r=\Gamma) + \frac{1}{r}\frac{\partial\tilde{u}_\theta}{\partial r}(r=\Gamma)$$
$$+\frac{1}{r^2}\tilde{u}_\theta(r=\Gamma) - im\frac{\mu}{r^2}\tilde{u}_\theta(r=\Gamma) = 0, \tag{B36}$$

by taking (B14) into account, the above expression simplifies to

$$\frac{1}{\Gamma}\frac{\partial u_\theta}{\partial r} = \frac{1}{\Gamma}\tilde{\zeta}(r=\Gamma) - \frac{1}{\Gamma^2}\tilde{u}_\theta(r=\Gamma) - \frac{im}{\Gamma^2}\tilde{u}_r(r=\Gamma), \tag{B37}$$

substituting (B37) into (B36), the dispersion relation is obtained as

$$i\chi\tilde{u}_\theta(r=\Gamma) + \frac{\tilde{\zeta}(r=\Gamma)}{\Gamma} = \frac{im}{\Gamma^2}[\tilde{u}_r(r=\Gamma) + \tilde{u}_\theta(r=\Gamma)], \tag{B38}$$

in (B38), the quantities $\tilde{u}_r(\Gamma)$, $\tilde{u}_\theta(\Gamma)$, and $\tilde{\zeta}(\Gamma)$ are determined from (B23), (B31), and (B35), which are summarized as

$$\tilde{\zeta}(r) = C\exp\left[\tfrac{i\chi}{2}(1-r^2) + im\mu\ln r\right],$$
$$\tilde{u}_r = -iC[F_\eta + G_\eta - r^{m-1}G_\eta(r=1)],$$
$$\tilde{u}_\theta = C[F_\eta - G_\eta + r^{m-1}G_\eta(r=1)]. \tag{B39}$$

The dispersion equation (B38) depends on the parameters m, Γ, μ, χ. We recall that, to evaluate the characteristics of the rotating instability at neutral condition, the imaginary part of ξ has already been set to zero, i.e., $\sigma = 0$. All numerical calculations were performed using the commercial software MATLAB.

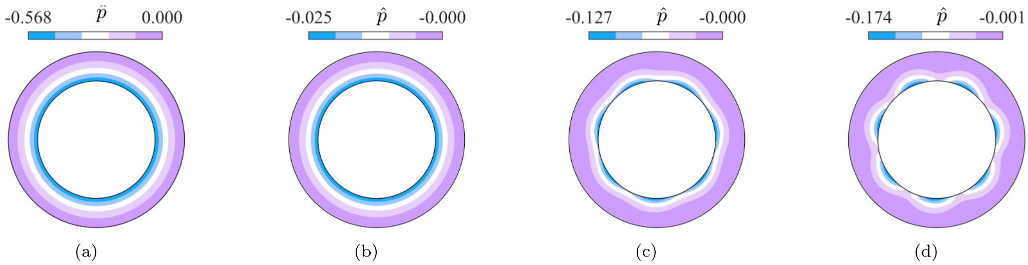

FIG. 19. Basic states of the diffuser flow with a radius ratio of $\Gamma = 1.50$: (a) results from the LSA model and URANS results under the critical flow condition ($\alpha = 8.14^\circ$, $\Phi = 0.625$) with a seven-periodic inflow Fourier mode with three different amplitudes: (b) $A = 0$, (c) $A = 0.15$, and (d) $A = 0.35$. The basic states in the URANS simulations are obtained by phase-averaging the static pressure field in a reference frame rotating with the inlet radial source flow modulation.

APPENDIX C: BASIC STATE OF THE LSA AND OF URANS MODEL

Figure 19 shows an example of the basic state of the LSA model and of our URANS simulation with a seven-periodic inflow Fourier with three different amplitudes. We further recall that the basic states in the URANS simulations are obtained by phase-averaging the static pressure field in a reference frame corotating with the inlet radial source flow modulation.

APPENDIX D: MORE DETAILS OF THE INSTABILITY CHARACTERISTICS CAPTURED BY THE 2D URANS MODEL

Figures 20–22 show more details of the instability characteristics captured by the 2D URANS model.

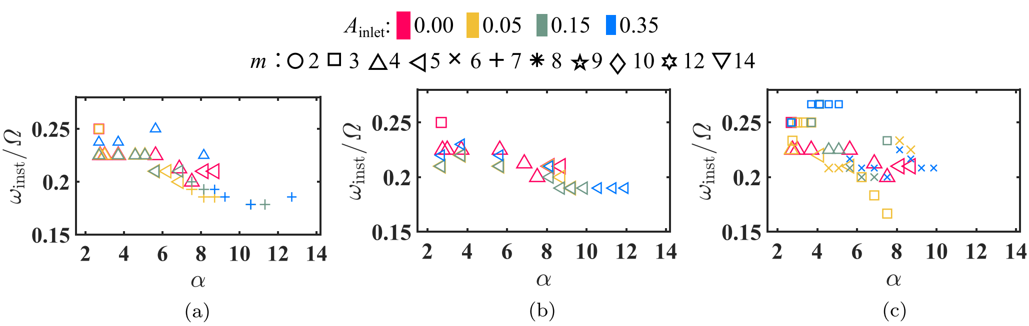

FIG. 20. Instability propagation velocity of the flow in the diffuser of radius ratio $\Gamma = 1.50$ with a periodic inflow Fourier mode with four different amplitudes A and three different Fourier-mode numbers m_{F}: (a) $m_{\mathrm{F}} = 7$, (b) $m_{\mathrm{F}} = 5$, and (c) $m_{\mathrm{F}} = 3$.

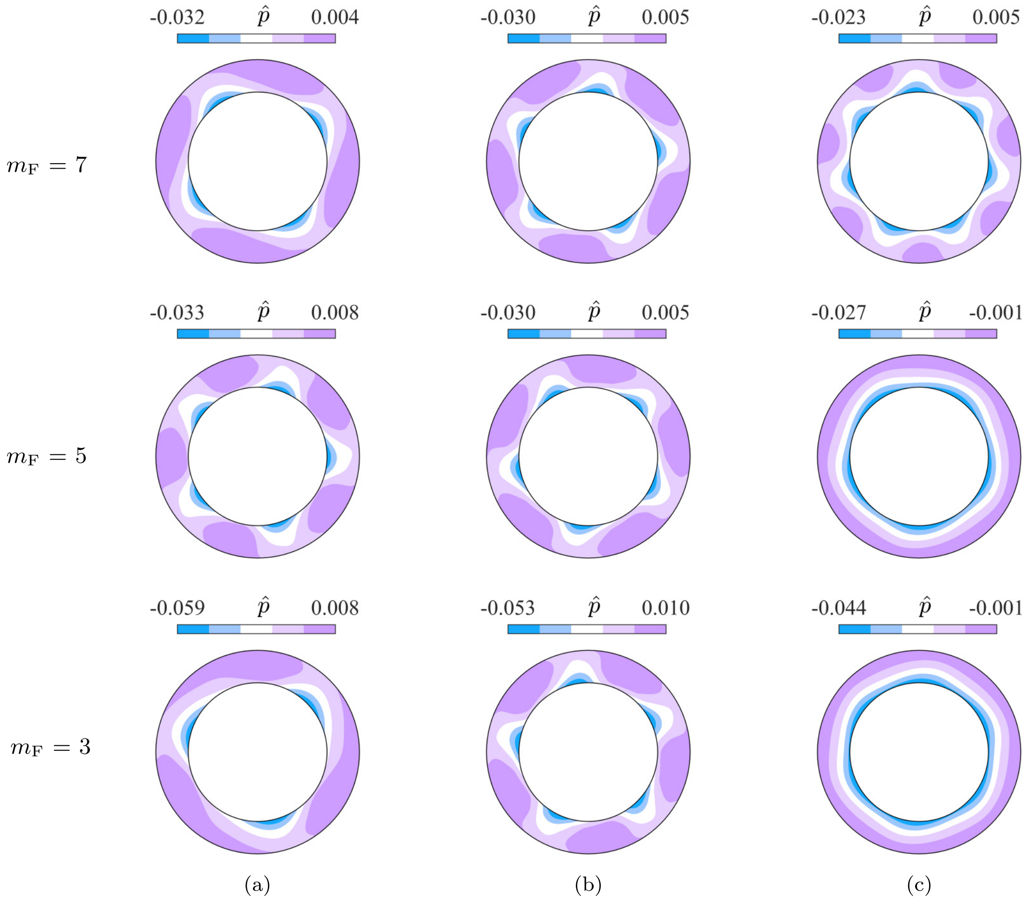

FIG. 21. Phase-averaged static pressure field for the diffuser of radius ratio $\Gamma = 1.50$ with a seven-periodic inflow Fourier mode $m_F = 7$ with an amplitude $A = 0.05$ in a reference frame rotating with the identified instability Fourier mode under different flow angles: (a) $\alpha = 3.69^\circ$ ($\Phi = 0.375$), (b) $\alpha = 5.63^\circ$ ($\Phi = 0.5$), (c) $\alpha = 8.14^\circ$ ($\Phi = 0.625$).

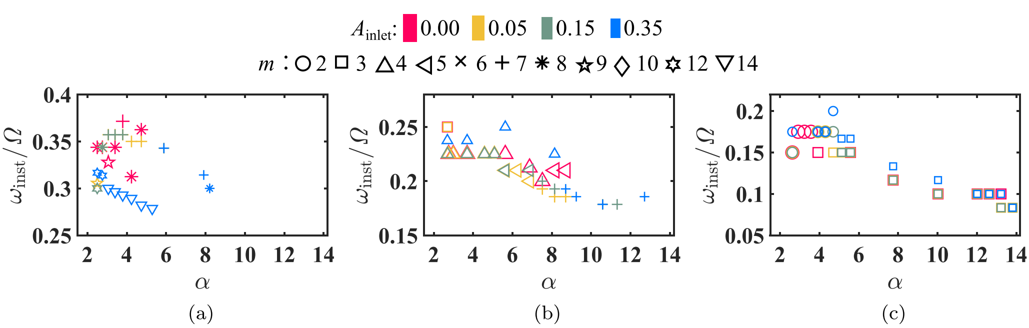

FIG. 22. Instability propagation velocity of the flow in the diffuser with a seven-periodic inflow Fourier mode with four different amplitudes A with three different radius ratios Γ: (a) $\Gamma = 1.25$, (b) $\Gamma = 1.50$, (c) $\Gamma = 2$.

[1] S. Mochizuki and W.-J. Yang, Self-sustained radial oscillating flows between parallel disks, J. Fluid Mech. **154**, 377 (1985).
[2] H. D. Murphy, M. Coxon, and D. M. McEligot, Symmetric sink flow between parallel plates, J. Fluids Eng. **100**, 477 (1978).
[3] M. Tabatabai and A. Pollard, Turbulence in radial flow between parallel disks at medium and low Reynolds numbers, J. Fluid Mech. **185**, 483 (1987).
[4] J. Raal, Radial source flow between parallel disks, J. Fluid Mech. **85**, 401 (1978).
[5] C. Hu, C. Yang, X. Shi, R. Zou, L. Liu, and H. Chen, Investigation of rotating stall in radial vaneless diffusers with asymmetric inflow, Aerosp. Sci. Technol. **96**, 105546 (2020).
[6] A. Dazin, O. Coutier-Delgosha, P. Dupont, S. Coudert, G. Caignaert, and G. Bois, Rotating instability in the vaneless diffuser of a radial flow pump, J. Therm. Sci. **17**, 368 (2008).
[7] A. Dazin, G. Cavazzini, G. Pavesi, P. Dupont, S. Coudert, G. Ardizzon, G. Caignaert, and G. Bois, High-speed stereoscopic PIV study of rotating instabilities in a radial vaneless diffuser, Exp. Fluids **51**, 83 (2011).
[8] T. Hagiwara, Studies on the characteristics of radial-flow nozzles: (1st report, theoretical analysis of outward flow), Bull. JSME **5**, 656 (1962).
[9] Y. Qin, J. Chen, X. Zhao, D. Liao, R. Mu, S. Wang, H. Wu, and H. Guo, Transcatheter closure of perimembranous ventricular septal defect using a modified double-disk occluder, Am. J. Cardiol. **101**, 1781 (2008).
[10] J. Hunt and I. Torbe, Characteristics of a hydrostatic thrust bearing, Int. J. Mech. Sci. **4**, 503 (1962).
[11] W. M. Kissling and C. Massiot, Modelling of flow through naturally fractured geothermal reservoirs, Taupō Volcanic Zone, New Zealand, Geotherm. Energy **11**, 20 (2023).
[12] H. A. Stone and H. Brenner, Dispersion in flows with streamwise variations of mean velocity: Radial flow, Ind. Eng. Chem. Res. **38**, 851 (1999).
[13] E. Bakket, J. Kreider, and F. Kreith, Turbulent source flow between parallel stationary and co-rotating disks, J. Fluid Mech. **58**, 209 (1973).
[14] J.-L. Peube, Sur l'ecoulement radial permanent d'un fluide viszuex incompressible entre deux plans paralleles fixes, J. Mec. **2**, 377 (1963).
[15] S. Mochizuki, S. Yamada, and H. Osaka, Management of a plane turbulent wall jet by the Large-Eddy Break-up device, JSME Int. J. Ser. B **49**, 921 (2006).
[16] X. Flete, N. Binder, Y. Bousquet, and S. Cros, Numerical investigation of rotating instability development in a wide tip gap centrifugal compressor, IJTPP **8**, 25 (2023).
[17] I. Day, Stall, surge, and 75 years of research, J. Turbomach. **138**, 011001 (2016).
[18] W. Jansen, Rotating stall in a radial vaneless diffuser, J. Basic Eng. **86**, 750 (1964).
[19] Y. Tsujimoto, Y. Yoshida, and Y. Mori, Study of vaneless diffuser rotating stall based on two-dimensional inviscid flow analysis, J. Fluids Eng. **118**, 123 (1996).
[20] S. Ljevar, H. C. D. Lange, and A. A. V. Steenhoven, Two-dimensional rotating stall analysis in a wide vaneless diffuser, Int. J. Rotating Mach. **2006**, 056420 (2006).
[21] G. Pavesi, A. Dazin, G. Cavazzini, G. Caignaert, G. Bois, and G. Ardizzon, Experimental and numerical investigation of unforced unsteadiness in a vaneless radial diffuser, in *9th European Conference on Turbomachinery: Fluid Dynamics and Thermodynamics, ETC 2011 - Conference Proceedings* (Istanbul Technical University, Istanbul, Turkey, 2011), Vol. 1.
[22] Y. Heng, A. Dazin, and M. Ouarzazi, Linear stability analysis of rotating stall in a wide vaneless diffuser, in *12th European Conference on Turbomachinery Fluid Dynamics and Thermodynamics, ETC 2017* (Euroturbo and KTH Royal Institute of Technology, Stockholm, Sweden, 2017).
[23] Y. Senoo, Y. Kinoshita, and M. Ishida, Asymmetric flow in vaneless diffusers of centrifugal blowers, J. Fluids Eng. **99**, 104 (1977).
[24] Y. Senoo and Y. Kinoshita, Influence of inlet flow conditions and geometries of centrifugal vaneless diffusers on critical flow angle for reverse flow, J. Fluids Eng. **99**, 98 (1977).

[25] H.-S. Dou and S. Mizuki, Analysis of the flow in vaneless diffusers with large width-to-radius ratios, J. Turbomach. **120**, 193 (1998).

[26] P. Frigne and R. Van den Braembussche, A theoretical model for rotating stall in the vaneless diffuser of a centrifugal compressor, J. Eng. Gas Turbines Power **107**, 507 (1985).

[27] A. Abdelhamid, Effects of vaneiess diffuser geometry on flow instability in centrifugal compression systems, *Turbo Expo: Power for Land, Sea, and Air* (American Society of Mechanical Engineers, New York, 1981), Vol. 79610, p. V001T03A008.

[28] F. Moore, Theory of finite disturbances in a centrifugal compression system with a vaneless radial diffuser, *Turbo Expo: Power for Land, Sea, and Air* (American Society of Mechanical Engineers, New York, 1991), Vol. 78989, p. V001T01A030.

[29] Y. G. Heng, A. Dazin, M. N. Ouarzazi, and Q. R. Si, A study of rotating stall in a vaneless diffuser of radial flow pump, J. Hydraul. Res. **56**, 494 (2018).

[30] M. Fan, A. Dazin, F. Romano, and G. Bois, Effect of leakage on the performance of the vaneless diffuser of a centrifugal pump model, *Conference on Modelling Fluid Flow (CMFF'22), Budapest, Hungary* 51 (Budapest University of Technology and Economics, Budapest, Hungary, 2022).

[31] M. Fan, A. Dazin, G. Bois, and F. Romanò, Effect of radius ratio on the instabilities in a vaneless diffuser, Eur. J. Mech. B/Fluids **104**, 1 (2024).

[32] M. Fan, A. Dazin, G. Bois, and F. Romanò, Instabilities identification based on a new centrifugal 3D impeller outflow model, Aerosp. Sci. Technol. **140**, 108466 (2023).

[33] M. Fan, A. Dazin, G. Bois, and F. Romanò, Effect of inlet leakage flow on the instability in a radial vaneless diffuser, Phys. Fluids **35**, 014105 (2023).

[34] M. Fan, A. Dazin, G. Bois, and F. Romanò, Instabilities in a turbulent swirling source flow between parallel rings, Phys. Fluids **35**, 101701 (2023).

[35] D. C. Wilcox, *Turbulence Modeling for CFD* (DCW Industries, La Canada, California, 1993).

[36] P. Sváček, P. Louda, and K. Kozel, On numerical simulation of three-dimensional flow problems by finite element and finite volume techniques, J. Comp. App. Math. **270**, 451 (2014).

[37] F. R. Menter, J. C. Ferreira, T. Esch, and B. Konno, The SST turbulence model with improved wall treatment for heat transfer predictions in gas turbines, in *Proceedings of the International Gas Turbine Congress* (Japan Society of Mechanical Engineers, Tokyo, Japan, 2003).

[38] M. Rahman, Numerical investigation of unsteady flow past a circular cylinder using 2-D finite volume method, J. Nav. Archit. Mar. Eng. **4**, 27 (2008).

[39] F. R. Menter, Ten years of industrial experience with the SST turbulence model, Turbulence, Heat and Mass Transfer **4**, 625 (2003).

[40] F. Cenci and A. L. C. Fujarra, URANS simulation: Numerical study of flow around a two dimensional circular cylinder, in *Proceedings of the XXXVIII Iberian Latin-American Congress on Computational Methods in Engineering* (Associação Brasileira de Métodos Computacionais em Engenharia, Rio de Janeiro, Brazil, 2017).

[41] F. R. Menter, Two-equation eddy-viscosity turbulence models for engineering applications, AIAA J. **32**, 1598 (1994).

[42] D. C. Wilcox *et al.*, *Turbulence Modeling for CFD* (DCW industries La Canada, CA, 1998), Vol. 2.

[43] C. Cambon, N. N. Mansour, and F. S. Godeferd, Energy transfer in rotating turbulence, J. Fluid Mech. **337**, 303 (1997).

[44] P. Spalart and M. Shur, On the sensitization of turbulence models to rotation and curvature, Aerosp. Sci. Technol. **1**, 297 (1997).

[45] M. Invigorito, D. Cardillo, and G. Ranuzzi, Application of OPENFOAM for rocket design, in *9th OPENFOAM Workshop* 1 (OpenFOAM Foundation Ltd., London, 2003).

[46] M. Šourek and M. Isoz, DEM-CFD study of flow in a random packed bed, Conference TOPICAL PROBLEMS OF FLUID MECHANICS (2018).

[47] D. Sipp and L. Jacquin, Three-dimensional centrifugal-type instabilities of two-dimensional flows in rotating systems, Phys. Fluids **12**, 1740 (2000).

[48] S. Suzuki, U. Yoshio, and H. H., Noise characteristics in partial discharge of centrifugal fans: 1st report, low-frequency noise due to the rotating stall, Bull. JSME **21**, 689 (1978).
[49] G. Caignaert, B. Desmet, and D. Stevenaert, Experimental investigations on the flow in the impeller of a centrifugal fan, *Turbo Expo: Power for Land, Sea, and Air* (American Society of Mechanical Engineers, New York, 1982), Vol. 79566, p. V001T01A013.